

# A new family of second order convergent weakly-compressible SPH schemes

Pawan Negi<sup>a,\*</sup>, Prabhu Ramachandran<sup>a</sup>

<sup>a</sup>*Department of Aerospace Engineering, Indian Institute of Technology Bombay, Powai, Mumbai 400076*

---

## Abstract

Despite the many advances in the use of weakly-compressible smoothed particle hydrodynamics (SPH) for the simulation of incompressible fluid flow, it is still challenging to obtain second-order convergence numerically. In this paper we perform a systematic numerical study of convergence and accuracy of kernel-based approximation, discretization operators, and weakly-compressible SPH (WCSPH) schemes. We explore the origins of the errors and issues preventing second-order convergence. Based on the study, we propose several new variations of the basic WCSPH scheme that are all second-order accurate. Additionally, we investigate the linear and angular momentum conservation property of the WCSPH schemes. Our results show that one may construct accurate WCSPH schemes that demonstrate second-order convergence through a judicious choice of kernel, smoothing length, and discretization operators in the discretization of the governing equations.

*Keywords:* SPH, Numerical Convergence, Accuracy, Conservation, Weakly-compressible fluid flow

---

## 1. Introduction

Smoothed Particle Hydrodynamics has been used to simulate weakly-compressible fluids since the pioneering work of Monaghan [1]. Many variations of the basic method have been proposed to create an entire class

---

\*Corresponding author

*Email addresses:* `pawan.n@aero.iitb.ac.in` (Pawan Negi),  
`prabhu@aero.iitb.ac.in` (Prabhu Ramachandran)

of weakly-compressible SPH schemes (WCSPH). One particularly difficult challenge has been the poor convergence displayed by the WCSPH methods making it one of the SPH grand-challenge problems [2].

The SPH method works by using a smoothing kernel to approximate a function wherein the choice of the kernel influences the accuracy of the method. The length scale of the smoothing kernel is often termed the support radius or smoothing length,  $h$ . A variety of kernels are used in the literature and the smoothing length may either be fixed in space/time or varying. One can show that for a symmetric kernel, the SPH kernel approximation is spatially second-order accurate in  $h$ . However, the particle discretization of this approximation seldom achieves this and even first-order convergence often requires care and tuning of the smoothing length. Hernquist and Katz [3] proposed that the support radius,  $h$  be increased such that  $h \propto \Delta s^{-1/3}$  in three dimensions where  $\Delta s$  is the local inter-particle separation. Subsequently, Quinlan et al. [4] derived error estimates for the standard SPH discretization and found that the ratio  $h/\Delta s$  must increase as the  $h$  value is reduced to attain convergence; this is because of error terms of the form  $(\frac{\Delta s}{h})^{\beta+2}$ , where  $\beta$  is a measure of the smoothness of the kernel at the edge of its support. This is an issue because as  $h$  increases, the number of neighbors for each particle increases resulting in a prohibitive increase of computational effort. Furthermore, increasing the smoothing radius also reduces the accuracy of the method. This is the approach used in the work of Zhu et al. [5] who proposed that the number of neighbors  $N_{nb} \propto N^{0.5}$ , where  $N$  is the number of particles, in order to get convergence using SPH kernels.

Kiara et al. [6, 7] shows that when the particles are distributed uniformly it is possible to obtain second-order convergence. The results of [4] show that when using sufficiently smooth kernels (where  $\beta$  is large or infinite), one can obtain second-order convergence. Indeed, Lind and Stansby [8] demonstrate that for particle distributions on a Cartesian mesh one can obtain higher order convergence using higher order kernels.

However, for kernels that are normally used in SPH, the SPH approximations of derivatives become inaccurate even on a uniform grid unless a very large smoothing radius is used. Many methods have been proposed to correct the gradient approximation [9, 10, 11, 12]. These typically ensure that the derivative approximation of a linear function is exact. This linear consistency is achieved by inverting a small matrix for each particle and using this to correct the computed gradients. This makes the derivative approximation

second-order accurate but increases the computational cost of the gradient computation two-fold.

In the context of incompressible fluid flows, the governing equations involve the divergence, gradient, and Laplacian operators. These operators must be discretized and used in the context of Lagrangian particles. The divergence operator is encountered in the continuity equation and the discretization proposed by [1] is widely used. Rather than using a continuity equation, some authors [13] prefer to use the summation density formulation proposed in [14] to directly evaluate density. The gradient operator is encountered in the momentum equation. Many authors prefer using a discretized form that manifestly preserves linear momentum and as a result employ the symmetric form of the gradient operator [1, 9]. The symmetrization can be done in two different ways and Violeau [15] shows that the selection of one form dictates the form to be used for divergence discretization in order to conserve volume (energy) in phase space.

Given the inaccuracy of the SPH approximation in computing derivatives accurately, the kernel corrections of [9, 10] maybe applied to obtain linear consistency of the gradient and divergence operators. Unfortunately, the use of the corrections implies that linear momentum is no longer manifestly conserved. Frontiere et al. [16] propose a symmetrization of the corrected kernel as originally suggested by Dilts [17, 18] to conserve linear momentum but the symmetrization implies that the operator is not first order consistent. Thus, the unfortunate consequence of demanding linear consistency is lack of conservation and vice-versa. A conservative and linear consistent gradient operator is currently not available.

The Laplacian is a challenging operator in the context of SPH. The simplest method is the one where the double derivative of the kernel is employed. However, the double derivatives of the kernel are very sensitive to any particle disorder. Chen and Beraun [19] propose an approach by considering the inner product with each of the double derivatives and taking into account the leading order error terms. Zhang and Batra [20] propose using the inner product with all the derivatives of the kernel lower and equal to the required derivative. This generates a system of 10 equations in two-dimensions. Korzilius et al. [21] propose an improvement over the method of [19] to evaluate the correction term. All of these methods require the computation of higher order kernel derivatives. Many authors [22, 23] proposed methods to correct the Laplacian near the boundary. In all of these formulations linear momentum is not manifestly conserved.

The Laplacian may also be discretized using the first derivative of the kernel using an integral approximation of the Laplacian. This was first suggested by [24] and has been improved by [25, 26]. They employ a finite difference approximation to evaluate the first order derivative and then convolve this with the kernel derivative. This formulation was structured such that it conserves linear momentum. However, these approximations do not converge as the resolution increases especially in the context of irregular particle distributions. Fatehi and Manzari [27] propose an improved formulation by accounting for the leading error term; this makes the method accurate and convergent but makes the approximations non-conservative.

Another method to discretize the Laplacian is the repeated use of a first derivative and this has been used by Bonet and Lok [9], and Nugent and Posch [28]. The formulation is generally not popular since it shows high frequency numerical oscillations when the initial condition is discontinuous. Recently, Biriukov and Price [29] show that these oscillations can be removed by employing smoothing near the discontinuity.

Various SPH schemes have been proposed that use the above methods for discretization of the different operators. The simplest of the schemes is the original weakly compressible SPH (WCSPH) method [1, 30]. This method is devised such that it conserves linear momentum as well as the Hamiltonian of the system. However, as the particles move they become highly disorganized and this significantly reduces the accuracy of the method. Many particle regularization methods popularly known as particle shifting techniques (PST) have been proposed which can be incorporated into WCSPH schemes [31, 32, 33, 12]. These methods ensure that the particles are distributed more uniformly. Instead of displacing the particles directly, Adami et al. [13] propose to use a transport velocity instead of the particle velocity to ensure a uniform particle distribution. This approach is also framed in the context of Arbitrary Lagrangian Eulerian (ALE) SPH schemes by [34]. A similar approach is used by Sun et al. [33] to incorporate the shifting velocity in the momentum equation with the  $\delta$ -SPH scheme [35, 36]. Ramachandran and Puri [37] also employ a transport velocity formulation and additionally propose using the EDAC scheme [38] in the context of SPH, which removes the need for an equation of state (EOS). The resulting method is accurate but does not converge with an increase of resolution. An alternative approach to ensure particle homogeneity is the approach of remeshing proposed by Chaniotis et al. [39] where the particles are periodically interpolated into a regular Cartesian mesh. The method can be accurate but the remeshing



can be diffusive and makes the method reliant on a Cartesian mesh. In a subsequent development, Hieber and Koumoutsakos [40] employ remeshing but couple it with an immersed boundary method to deal with complex solid bodies. Recently, Nasar et al. [41] modify the method introduced by Lind et al. [32] to devise an Eulerian WCSPH scheme that also uses ideas from immersed boundary methods to handle complex geometry.

To summarize the discussion in the context of convergence, some authors [4, 22, 23] demonstrate numerical convergence for the derivative and function approximation. Many authors [7, 12, 13, 19, 20, 42, 35] only show convergence in the form of plots that approach an exact solution with increasing resolution without formally computing the order of convergence. Some authors demonstrate second order convergence for simpler problems with a fixed particle configuration like the heat conduction equation [26, 22, 27, 21], the Poisson equation [23], and the evolution of an acoustic wave [16]. Second order convergence has also been demonstrated for Eulerian SPH methods where the particles are held fixed [8, 41] or where the particles are re-meshed [40]. Some authors [11, 16, 31, 43, 37, 44] show first order convergence for Lagrangian SPH schemes but this does not persist as the resolution is increased. Therefore, to the best of our knowledge, none of the contemporary Lagrangian SPH schemes appear to demonstrate a formal second order convergence for simple fluid mechanics problems like the Taylor-Green vortex problem for which an exact solution is known.

In this paper, we carefully construct a family of Lagrangian SPH schemes that demonstrate second order numerical convergence for the classic Taylor-Green vortex problem. We first study several commonly used SPH kernels in the context of function and derivative approximation using particles that are either in a Cartesian arrangement or in an irregular but packed configuration of particles encountered when employing some form of a particle shifting technique. We choose a suitable correction scheme that produces second order approximations. We then select a suitable kernel and smoothing radius based on this study. We then systematically study the various discretization operators along with suitable corrections. Our investigations are in two-dimensions although the results are applicable in three dimensions as well. Our numerical investigation covers a wide range of resolutions with our highest resolution using a quarter million particles with  $\frac{L}{\Delta_s} = 500$ , where  $L = 1m$  is the length of the domain. Once we have identified suitable second order convergent operators we carefully construct SPH schemes that display a second order convergence (SOC). We use the Taylor-Green vortex prob-

lem to demonstrate this. We also compare our results with those of several established SPH methods that are currently used. We study the accuracy, convergence, and also investigate the computational effort required. We construct both Lagrangian and Eulerian schemes that are fully second order convergent. We provide schemes that use either an artificial compressibility in the form of an equation of state or using a pressure evolution equation.

Once we have demonstrated second order convergence for the Taylor-Green vortex problem we proceed to investigate the Gresho-Chan vortex [45] problem as well as an incompressible shear layer problem [46] and look at how the lack of manifest conservation impacts the conservation of linear and angular momentum. In the interest of reproducibility, all the results shown in the paper are automatically generated through the use of an automation framework [47], and the source code for the paper is available at [https://gitlab.com/pypr/convergence\\_sph](https://gitlab.com/pypr/convergence_sph). In the next section we discuss the SPH method briefly and then proceed to look at the SPH kernel interpolation.

## 2. The SPH method

We define the SPH approximation of any scalar (vector) field  $f$  ( $\mathbf{f}$ ) in a domain  $\Omega$  by

$$\langle f(\mathbf{x}) \rangle = \int_{\Omega} f(\tilde{\mathbf{x}}) W(\mathbf{x} - \tilde{\mathbf{x}}, h) d\tilde{\mathbf{x}}, \quad (1)$$

where  $\mathbf{x}, \tilde{\mathbf{x}} \in \Omega$ ,  $W$  is the kernel function, and  $h$  is the support radius of the kernel. It is well known [48, 15] that for a suitably chosen quadrature rule and a symmetric kernel which satisfies  $\int W(\mathbf{x}) d\mathbf{x} = 1$  that,

$$f(\mathbf{x}) = \langle f(\mathbf{x}) \rangle + O(h^2). \quad (2)$$

Some of the widely used kernels are Gaussian [48], cubic spline [1], quintic spline, and Wendland quintic [49]. We note that in this work we take  $h$  to be a constant.

When the kernel support is completely inside the domain boundary then we can evaluate the gradient of a function by taking the gradient of the kernel inside the integral. This approximation is also second-order in  $h$  [15]. We discretize the domain  $\Omega$  using particles having mass  $m$ , and density  $\rho$ . The discretization of the domain into particles introduces additional error in the approximation and is discussed in Quinlan et al. [4]. We can approximate

the gradient of  $f$  as,

$$\nabla f(\mathbf{x}_i) = \sum_j f(\mathbf{x}_j) \nabla W_{ij} \omega_j + O(h^2) + O\left(\left(\frac{\Delta s}{h}\right)^{\beta+4}\right), \quad (3)$$

where  $W_{ij} = W(\mathbf{x}_i - \mathbf{x}_j, h)$ ,  $\omega_j = \frac{m_j}{\rho_j}$  is a measure of the volume of the particle,  $\beta$  is the smoothness of the kernel at the edge of its support, and the sum is taken over all the particles under the support of the kernel. The value of  $\beta$  is defined as the smallest order of derivative of the kernel at the edge of its support that is non-zero. For example,  $\beta = 3$  for cubic spline kernel, and  $\beta = 5$  for quintic spline kernel.

We note that the numerical volume  $\omega$  is an approximation and solely depends upon the spatial distribution of the particles. The density  $\rho$  may be computed for a particle using the summation density as,

$$\rho_i = \sum_j m_j W_{ij}. \quad (4)$$

Therefore, for constant mass we may write the volume as,

$$\omega_j = \frac{1}{\sum_j W_{ij}}. \quad (5)$$

Since the function and its derivative approximation depends on the kernel  $W$ , support radius  $h$ , and the scaling factor  $h_{\Delta s} = h/\Delta s$ , we perform a numerical study of the effect of the kernel in the next section.

### 3. Comparison of kernels

In this section, we compare various SPH kernels for their accuracy and order of convergence in a discrete domain. We evaluate the error in function and its derivative approximation in a two-dimensional periodic domain. We simulate periodicity by copying the appropriate particles and their properties near the boundary such that the boundary particles have full support [50]. The particles are either placed in a uniform mesh (unperturbed) or in a *packed* arrangement referred as unperturbed periodic (UP) or perturbed periodic (PP), respectively. In order to obtain the packed configuration, the particles are slightly perturbed from a uniform mesh and their positions are moved and allowed to settle into a distribution with a nearly constant density using

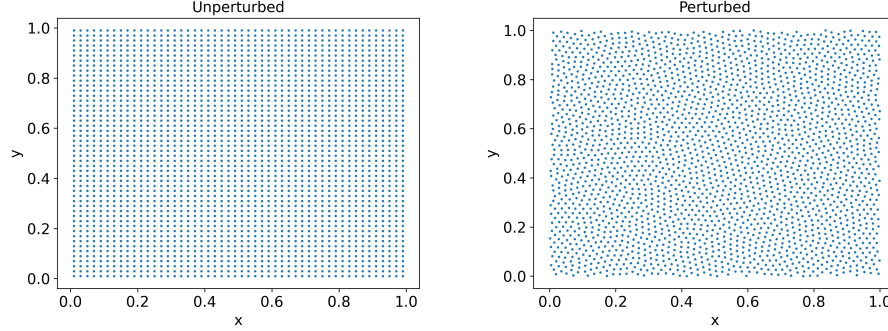


Figure 1: The unperturbed periodic particle and perturbed periodic particles.

a particle packing algorithm [51]. The algorithm effectively ensures that the particles are not clustered and have minimal density variations. It mimics the effect of many recent particle shifting algorithms [52, 32, 12]. In the fig. 1, we show both the domains.

Name	Radius	$\beta$	Remark
$G$ - Gaussian [48]	3	0	Truncated for low $N_{nbr}$
$QS$ - Quintic spline [37]	3	3	Tensile instability
$CS$ - Cubic spline [48]	2	5	Pairing and tensile instability
$WQ_2$ - Wendland $O(2)$ [49]	2	5	No tensile or pairing instability
$WQ_4$ - Wendland $O(4)$ [49]	2	8	Produces higher accuracy
$WQ_6$ - Wendland $O(6)$ [49]	2	11	Produces higher accuracy

Table 1: Kernels and their properties

In this paper, we compare the set of kernels listed in table 1. The set of kernels considered covers a wide range (high order, kernels having tensile instability and pairing instability [44, 53]). In order to assess the effect of  $h_{\Delta s}$  for a kernel, we perform the numerical experiment proposed by Dehnen

and Aly [44]. We evaluate particle density using eq. (4) for increasing the number of neighbors  $N_{nbr}$ , for each of the kernels. The increase in  $N_{nbr}$  corresponds to the scaling of the smoothing kernel using the  $h_{\Delta s}$  parameter. In this numerical experiment, we change both the resolution and  $h_{\Delta s}$ .

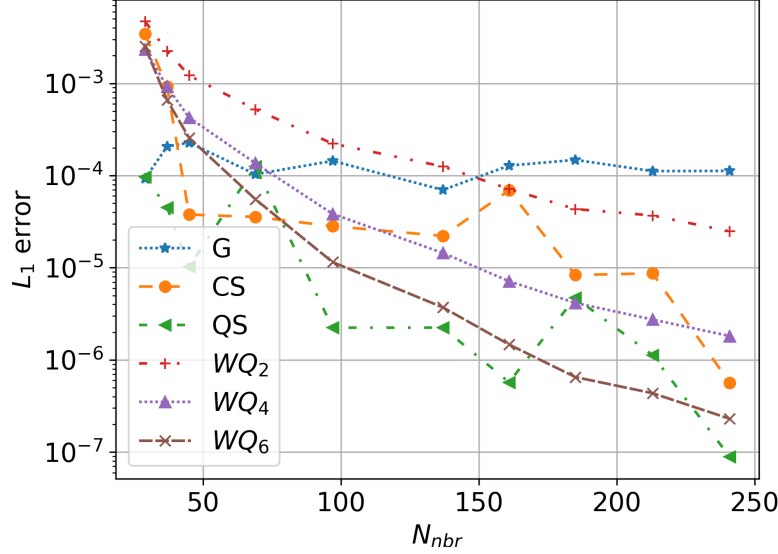


Figure 2: The particle density for different kernels with varying number of neighbors

In the fig. 2, we plot the absolute error in the particle density of one particle in an UP domain for different kernels with the change in  $N_{nbr}$  under the kernel support. Clearly, the Wendland class of kernel shows a monotonic decrease in error with the increasing  $N_{nbr}$ . However, in the case of the  $G$  and  $QS$  kernels, the errors are an order less at a lower  $N_{nbr}$  compared to Wendland class of kernels. The error in the  $G$  kernel does not change significantly with the change in the  $N_{nbr}$  compared to others. It is because we truncate the  $G$  kernel to have compact support. In the  $QS$ , the error is lower than the  $WQ_4$  in the entire plot. Therefore, we drop  $WQ_2$  and  $WQ_4$  in the subsequent investigations since it reaches the order of accuracy of  $QS$  when  $N_{nbr}$  is approximately 60. High  $N_{nbr}$  results in higher computational cost.

We compare the four kernels  $G$ ,  $CS$ ,  $QS$  and  $WQ_6$  for convergence of function and its gradient approximation. We consider the field,

$$f = \sin(\pi(x + y)). \quad (6)$$

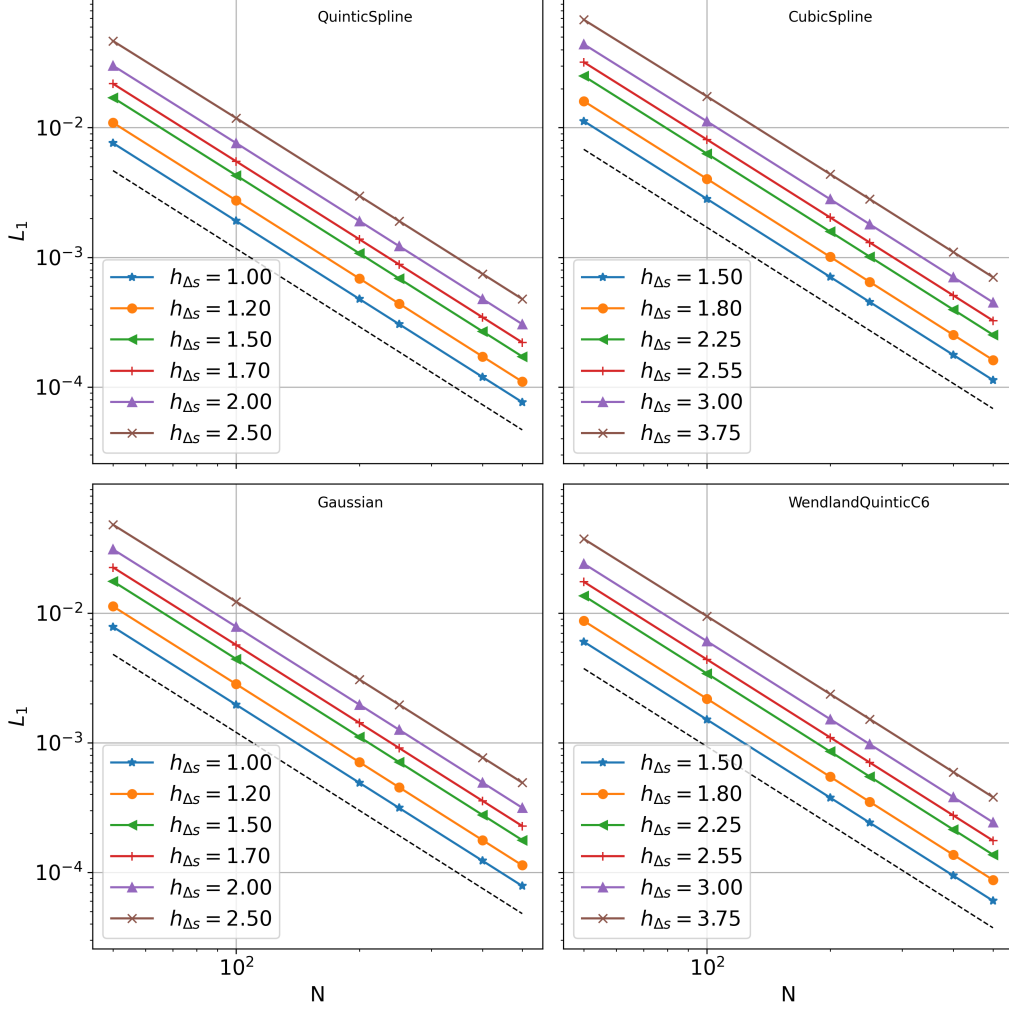


Figure 3: Order of convergence for the approximation of a function for different  $h_{\Delta s}$  values in an UP domain. The dashed line shows the second order rate.

Given a function  $g_o$  and its approximation  $g$ , we evaluate the  $L_1$  error using,

$$L_1 = \frac{\sum_i^N |g(\mathbf{x}_i) - g_o(\mathbf{x}_i)|}{\sum_i^N g_o(\mathbf{x}_i)}, \quad (7)$$

where  $N$  is the total number of particles in the domain. Since the  $CS$  and  $WQ_6$  kernels have support radius of 2 whereas, the  $G$  and  $QS$  kernel have support radius of 3, we set the  $h_{\Delta s}$  such that the  $N_{nbr}$  is same in an UP

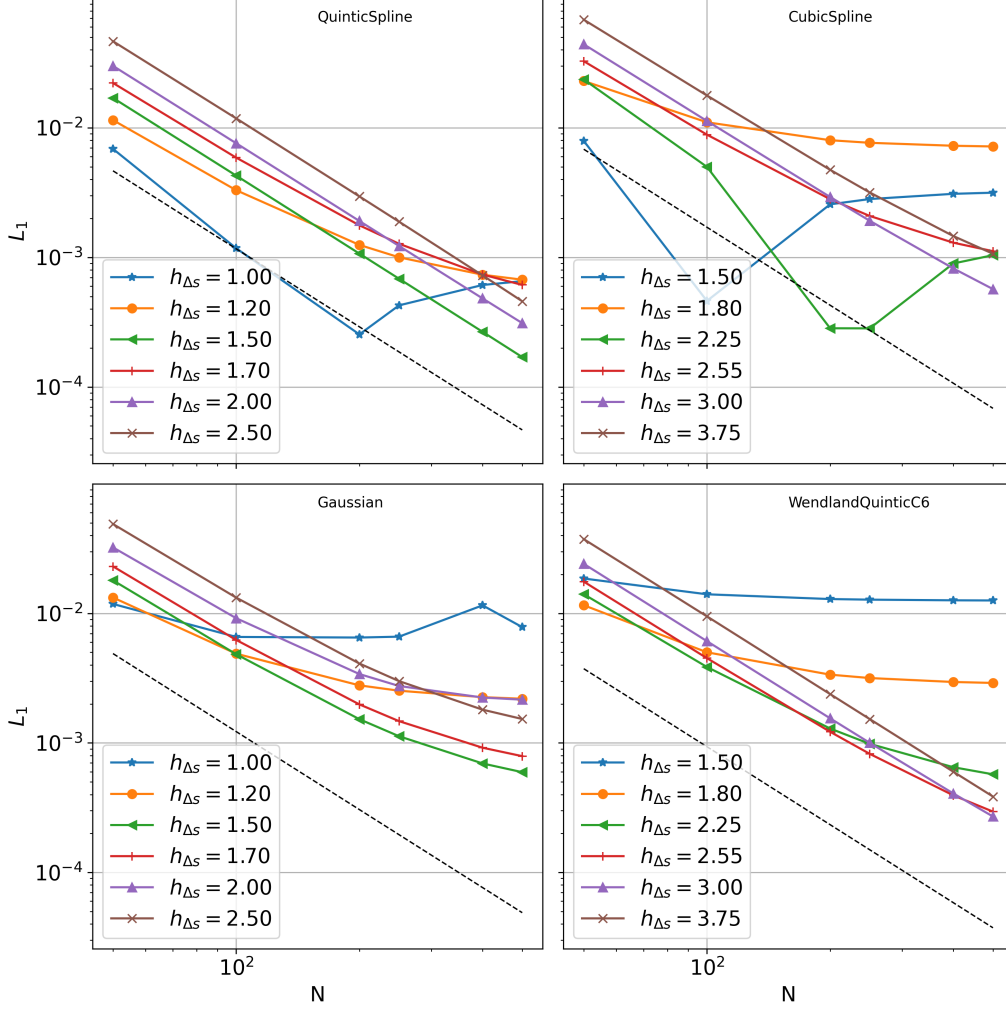


Figure 4: Order of convergence for derivative approximation for different  $h_{\Delta s}$  values in an UP domain. The dashed line shows the second order rate.

domain. Therefore, when  $h_{\Delta s} = 1.0$  for  $QS$  (or  $G$ ), we take  $h_{\Delta s} = 1.5$  for the  $CS$  (or  $WQ_6$ ). For the convergence study, in this paper, we consider  $50 \times 50$ ,  $100 \times 100$ ,  $200 \times 200$ ,  $250 \times 250$ ,  $400 \times 400$ , and  $500 \times 500$  resolutions for all the test cases unless stated otherwise.

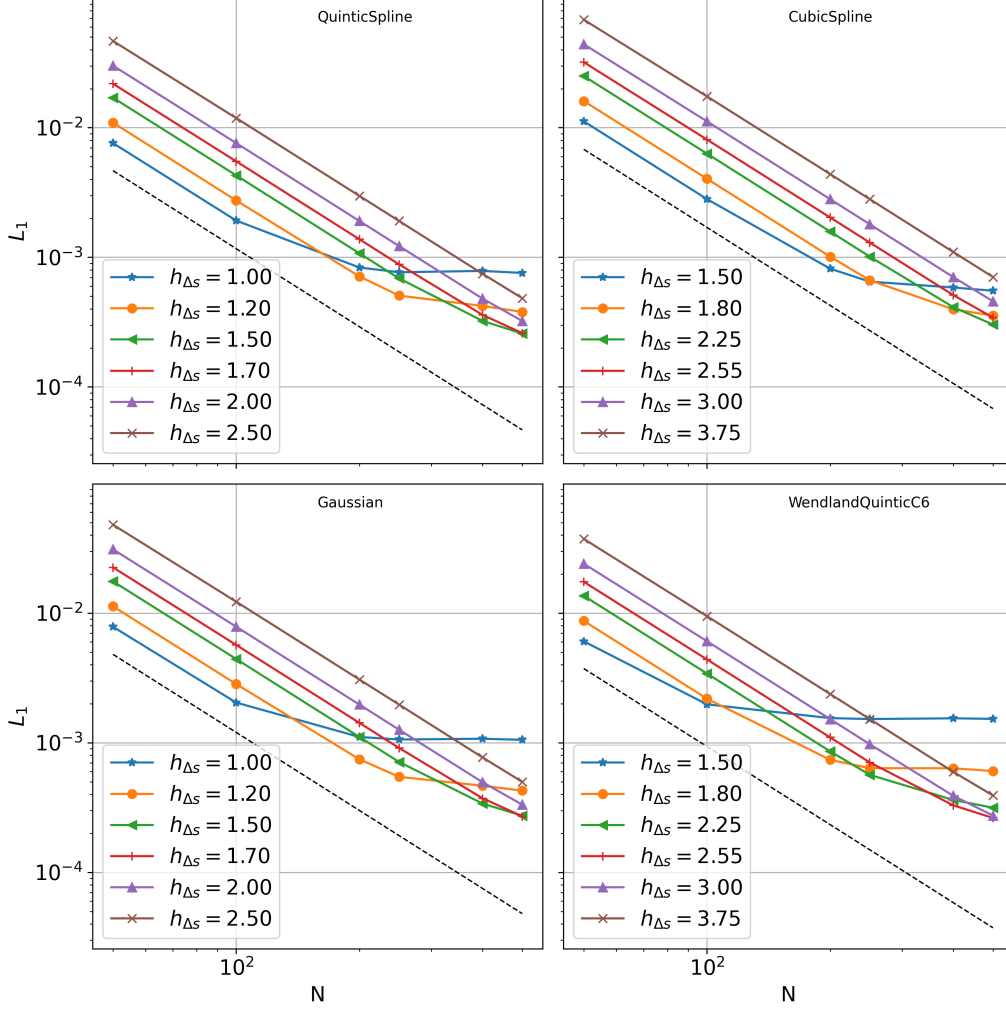


Figure 5: Order of convergence for function approximation for different  $h_{\Delta s}$  values in a PP domain. The dashed line shows the second order rate.

### 3.1. Unperturbed periodic domain

In fig. 3, we plot the  $L_1$  in the function approximation as a function of the resolution for different values of  $h_{\Delta s}$  in a UP domain. We observe similar error values for all the kernels except *CS*. We obtain second-order convergence (SOC) in an UP domain upto a considerably high resolution of  $500 \times 500$  as expected, for all the kernels [6].

In fig. 4, we plot the  $L_1$  error in the derivative approximation of the



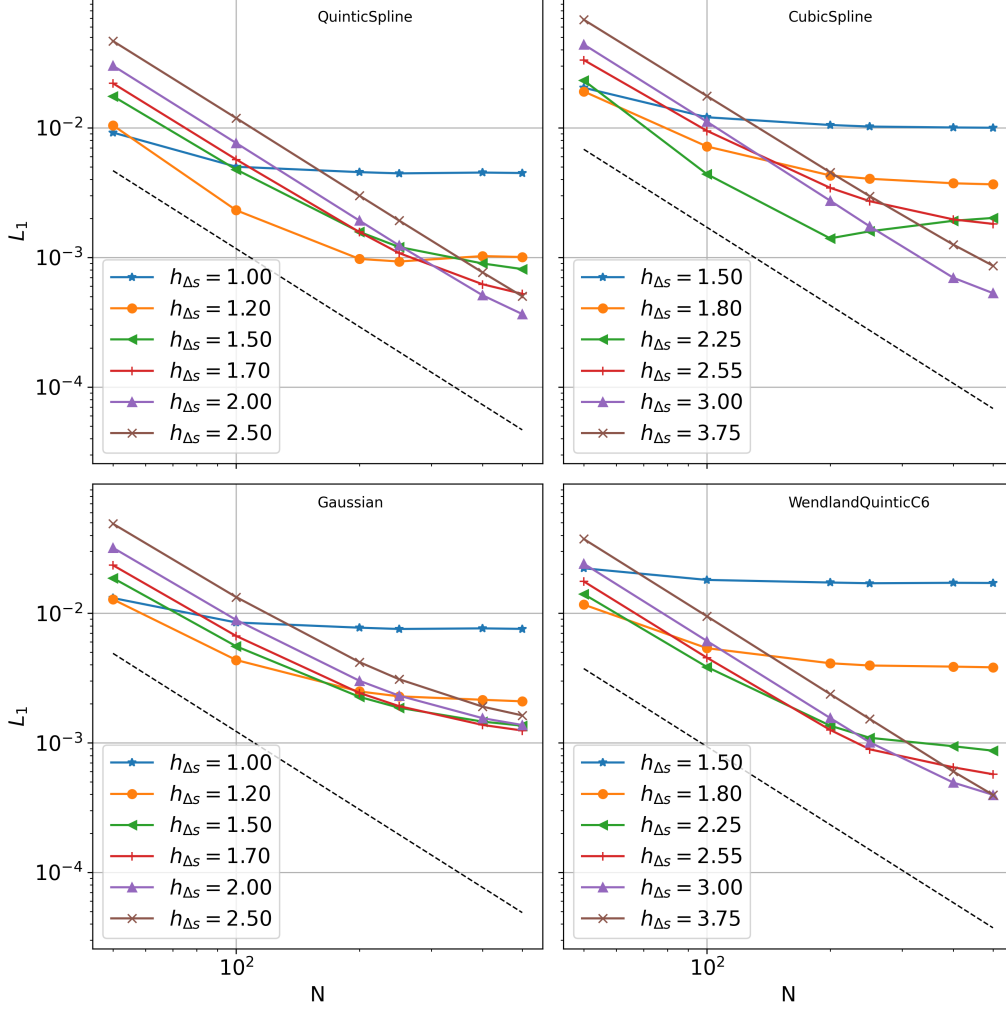


Figure 6: Order of convergence for the derivative approximation for different  $h_{\Delta s}$  values in a PP domain. The dashed line shows the second order rate. The eq. (8) is used for the approximation.

function in eq. (6) in a UP domain. The  $G$  and  $QS$  kernels show a better convergence rate compared to  $CS$  and  $WQ_6$  for lower  $h_{\Delta s}$ . The  $G$  kernel does not show SOC even at  $h_{\Delta s} = 2.5$ , since we use a truncated Gaussian. The  $CS$  and  $WQ_6$  kernel shows SOC only when  $h_{\Delta s} \geq 3.0$ . The  $QS$  kernel shows SOC at  $h_{\Delta s} > 1.5$  however, a reasonable convergence can be seen for  $h_{\Delta s} = 1.2$  as well.

### 3.2. Perturbed Periodic domain

In an SPH simulation, the particles advect with different velocities, and thus the distribution of particles is no longer uniform. Some particle shifting techniques (PST) can be used to make the particle distribution uniform [31, 32]. Thus, it is essential to observe the convergence rate in the PP domain as well.

In fig. 5, we plot the  $L_1$  error of the approximation of the field given in eq. (6) as a function of resolution in a PP domain for different  $h_{\Delta s}$  values. The convergence rates tend to zero for higher resolution for low value of  $h_{\Delta s}$  for all the kernels. The  $WQ_6$  kernel performs worse than the  $CS$  kernel at lower  $h_{\Delta s}$  values however, the errors are significantly lower in  $WQ_6$  when the  $h_{\Delta s}$  value increase. On comparing  $G$  and  $QS$ , the error plot looks exactly same except when  $h_{\Delta s} = 1.0$ .

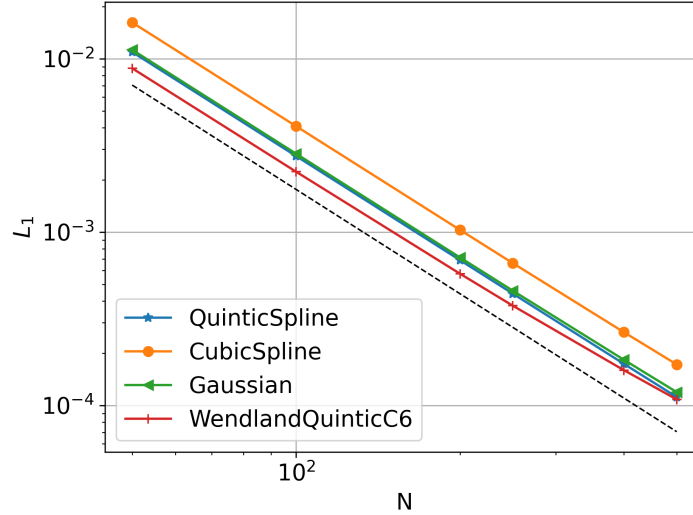


Figure 7: The convergence of the derivative approximation with different kernels when the gradient correction of Bonet and Lok [9] is used on a PP domain. Here we use  $h_{\Delta s} = 1.2$ .

The SPH approximation of the gradient of a function is not even zero order accurate in a perturbed domain [54, 6]. The derivatives diverge when we evaluate it using eq. (3). We use a zero order consistent method proposed by Monaghan [1] to compare the kernels. We write this approximation as,

$$\langle \nabla f(\mathbf{x}_i) \rangle = \sum_j (f(\mathbf{x}_j) - f(\mathbf{x}_i)) \nabla W_{ij} \omega_j. \quad (8)$$

In fig. 6, we plot the  $L_1$  error in the function derivative approximation as a function of resolution using eq. (8) in a PP domain for different  $h_{\Delta s}$  values and kernels. Clearly, the approximation for all the kernels shows at least zero-order convergence. The  $G$  kernel does not show SOC for high  $h_{\Delta s}$  which is the same as observed in the case of the UP domain. The accuracy in the case of  $QS$  and  $CS$  oscillates when going from lower  $h_{\Delta s}$  to higher values. Zhu et al. [5] suggest that one should increase the  $h_{\Delta s}$  as one increases the resolution but given the inconsistent behavior of the  $CS$  and  $QS$  kernels; these may not be suitable for that approach. The zero-order convergence rate occurs due to dominance of discretization error (the term  $(\frac{\Delta s}{h})^{\beta+4}$  in eq. (3)) when the resolution increases in the PP domain.

In order to observe the effect of kernel gradient correction, we apply the correction proposed by Bonet and Lok [9] for all the kernels. In fig. 7, we plot the  $L_1$  error in the derivative approximation as a function of resolution. Clearly, all the kernels  $G$ ,  $WQ_6$ ,  $CS$ , and  $QS$  show more or less the same behavior. Thus, we can choose any of these kernels for our convergence study of the WCSPH schemes. In the figure, it can be seen that the  $WQ_6$  and  $G$  kernels do not sustain the second-order behavior. Therefore in this work, we choose the  $QS$  kernel with  $h_{\Delta s} = 1.2$  for all the test cases henceforth.

#### 4. Comparison of SPH discretization operators

The SPH method is widely used to solve fluid flow problems. In this work, we focus on weakly-compressible SPH schemes that are used to simulate incompressible fluid flows. We write the Navier-Stokes equation for a weakly compressible flow along with the equation of state (EOS) as,

$$\begin{aligned}\frac{d\varrho}{dt} &= -\varrho \nabla \cdot \mathbf{u}, \\ \frac{d\mathbf{u}}{dt} &= -\frac{\nabla p}{\varrho} + \nu \nabla^2 \mathbf{u}, \\ p &= p(\varrho, \varrho_o, c_o),\end{aligned}\tag{9}$$

where  $\varrho$ ,  $\mathbf{u}$ , and  $p$  are the fluid density, velocity, and pressure, respectively,  $\nu$  is the kinematic viscosity,  $\varrho_o$  is the reference fluid density, and  $c_o$  is the artificial speed of sound in the fluid.

*Remark.* We note that the fluid density,  $\varrho$  is independent of the summation density  $\rho$ . Normally, in SPH simulations these two are treated as the same

Name	Expression	Used in
<b>sym1</b>	$\frac{(p_j+p_i)}{\rho_i\rho_j}\nabla W_{ij}m_j$	$\delta^+$ SPH [55]
<b>sym2</b>	$m_j\left(\frac{p_j}{\rho_j^2} + \frac{p_i}{\rho_i^2}\right)\nabla W_{ij},$ $\frac{V_i^2+V_j^2}{m_i}\tilde{p}_{ij}\nabla W_{ij}$	WCSPH [30], TVF [13, 57, 37], ISPH [58]
<b>asym</b>	$\frac{(p_j-p_i)}{\varrho_i}\nabla W_{ij}\omega_j$	WCSPH [48]

Table 2: Different gradient approximations for  $\frac{\nabla p}{\varrho}$ . The column “expression” is assumed to be summed over the index  $j$  over all the neighbor particles inside the kernel support. The term  $\varrho = \rho$  for gradient comparison.  $\tilde{p}_{ij} = \frac{p_i\rho_i+p_j\rho_j}{\rho_i+\rho_j}$  is the density averaged pressure.

and we discuss the reasons behind this choice in section 5. The property,  $\varrho$  does not depend upon particle configuration and should be prescribed as an initial condition.

For a scheme to be SOC, the SPH discretization of the RHS of all the equations in eq. (9) must be  $O(h^2)$ . Thus, in this section, we perform the comparison of the schemes by comparing the convergence of different approximations for the gradient, divergence, and Laplacian operators.

There are many different ways to discretize the momentum equation as can be seen from [30, 55, 13, 15, 16, 56]. One of the key features of the discretization of the momentum equation is to ensure linear momentum conservation. However, some researchers trade conservation for better accuracy [56] and others use a conservative form but chose to loose accuracy [16]. In view of this, we consider both conservative and non-conservative discretization in the present study.

#### 4.1. Comparison of $\frac{\nabla p}{\varrho}$ approximation

In this section, we compare various pressure gradient approximations. In the table 2, we list the gradient approximations considered in this study. The **sym1** and **sym2** are the symmetric, conservative form of the gradient approximation. We note that conservative forms have  $\varrho = \rho$ . The **asym** is the asymmetric form. Since the SPH kernel gradient does not show SOC in a perturbed domain [4], we also consider the kernel correction employed to each of the approximation. In this paper, we refer to the correction proposed

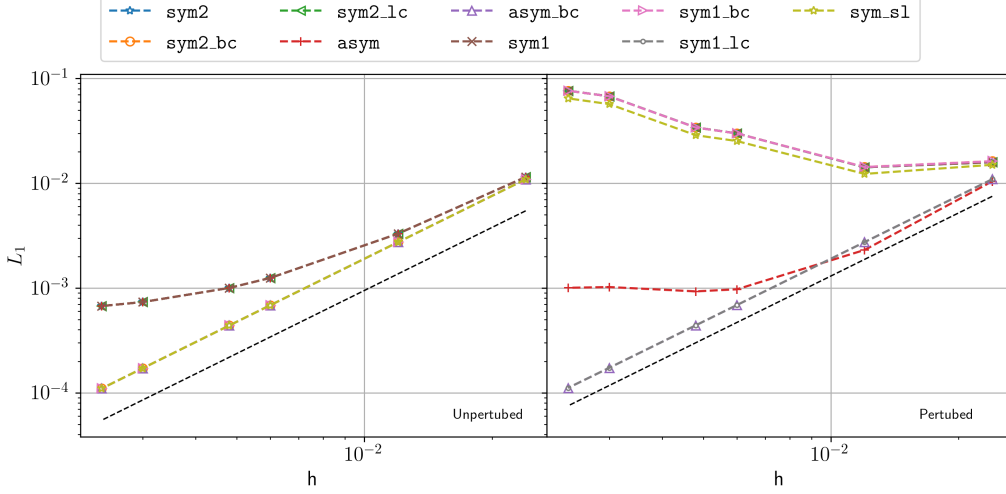


Figure 8: The rate of convergence in UP (left) and PP(right) domains for various pressure gradient listed in table 2. The dashed line shows the SOC rate. The `.bc` and `.lc` suffixes represent the corresponding form with Bonet correction [9] and Liu correction [10]. The `sym.sl` is the `sym1` formulation with symmetrization of kernel proposed in Diltz [17]

Name	$\frac{F_T}{F_{max}}$	$T_r$	$L_1$ error	Order
<code>asym.bc</code>	1.01e-02	1.97	1.11e-04	1.99
<code>asym</code>	3.10e-04	1.00	1.01e-03	0.98
<code>sym1.bc</code>	1.08e-02	1.87	7.65e-02	-0.75
<code>sym1.lc</code>	1.01e-02	2.35	1.11e-04	1.99
<code>sym1</code>	-2.53e-11	1.05	7.65e-02	-0.76
<code>sym2.bc</code>	1.10e-02	1.87	7.65e-02	-0.75
<code>sym2.lc</code>	-1.90e-11	2.43	7.65e-02	-0.76
<code>sym2</code>	-1.87e-11	1.01	7.65e-02	-0.76
<code>sym.sl</code>	-1.73e-11	2.50	6.46e-02	-0.72

Table 3: The ratio  $\frac{F_T}{F_{max}}$  showing the total force in the system due to lack of conservation in the approximation, the time taken  $T_r$  relative to the `asym` formulation, the  $L_1$  error for  $500 \times 500$  particle in a PP domain, and last column shows the order of convergence for all the kind of formulations considered in the first column.

by Bonet and Lok [9] as *Bonet correction* and the one proposed by Liu and Liu [10] as *Liu correction*. We add the suffix `_bc`, and `_lc` respectively in the plots and tables to indicate these corrections. The application of corrections renders the symmetric forms non-conservative, we use the method of symmetrization of the kernel proposed by Dilts [17] to again make it conservative. We refer to this formulation as `sym_s1` which we write as

$$\sum_j m_j \frac{p_j + p_i}{\rho_j \rho_i} (L_i \nabla W_{ij} - L_j \nabla W_{ji}), \quad (10)$$

where  $L_i$  is the Liu correction applied to the kernel gradient <sup>1</sup>. This formulation is used in the scheme proposed by Frontiere et al. [16].

In order to compare the convergence, we consider a pressure field,  $p = \sin(\pi(x + y))$ . We determine the  $L_1$  error using eq. (7), where  $g(\mathbf{x}_i)$  is the pressure gradient evaluated using the approximation and  $g_o(\mathbf{x}_i)$  is the exact pressure gradient. The exact pressure gradient,  $\nabla p = \pi \cos(\pi(x + y))(\hat{\mathbf{i}} + \hat{\mathbf{j}})$ . We compare only the x-component of the results. In fig. 8, we plot the error in the various gradient approximations discussed above in both an UP and PP domain. In the UP domain, barring the `sym2_lc`, all the corrected gradient approximations behave the same, whereas the uncorrected gradients do not display SOC. The corrected versions retains SOC even at high resolution since it reduces the discretization error in the approximation [27, 4]. We also observe that with the correction the second term involving the  $p_i$  term is zero in an UP domain leading to the same expression.

In the case of the PP domain, we observe that both `sym1` and `sym2` and their corresponding `_bc` versions overlap. The symmetric formulations show an increase in the error in the approximation with increasing resolution as suggested in Fatehi and Manzari [27]. Furthermore, the Bonet correction does not correct the symmetric formulations. Clearly, the `asym` formulation shows better convergence, and the Bonet correction version shows SOC. Therefore, the Bonet correction can be applied only when an asymmetric formulation is employed. Moreover, the Liu correction only corrects the symmetric form `sym1`, which suggests that the `sym2` cannot be corrected using traditional correction techniques. We investigate this in more detail in Appendix A. Finally, the `sym_s1` method has a slightly lower error but loses SOC behavior

---

<sup>1</sup>We select the `sym1` formulation over `sym2` as the latter does not perform well with the linear correction c.f Appendix A for details.

due to the symmetrization of the kernel gradient. Frontiere et al. [16] reported the similar behavior.

We also compare the linear momentum conservation and time taken to evaluate the gradient for the case with  $500 \times 500$  particles. As shown in Bonet and Lok [9], linear momentum is conserved when the total force,  $\sum_i F_i = 0$ , where the sum is taken over all the particles and  $F_i = \frac{\nabla p_i}{\rho_i}$ . In table 3, we tabulate the ratio of total force to the maximum force ( $\max(F_i)$ ), the time taken to evaluate the gradient scaled by the minimum time taken by all the methods, and the  $L_1$  error with the order of convergence <sup>2</sup>, for all the formulations plotted in fig. 8. As expected, all the symmetric forms of approximation have zero total force. The asymmetric formulation has a very small total force. Clearly, the use of Bonet corrections increases the total force and slows down the computation by a factor of 2, whereas the Liu correction makes it 2.4 times slower. The `sym_sl` formulation shows zero residual force as expected. Using the table 3, we can see that `asym_bc` and `sym1_lc` show SOC and have a very low total force which makes them a suitable candidate for a scheme with SOC.

#### 4.2. Comparison of $\nabla \cdot \mathbf{u}$ approximation

A zero order consistent SPH approximation for the divergence operator [48] is,

$$\nabla \cdot \mathbf{u} = \sum_j (\mathbf{u}_j - \mathbf{u}_i) \cdot \nabla W_{ij} \omega_j. \quad (11)$$

We refer to the approximation given in eq. (11) as `div`. We apply the Bonet correction as done in the case of gradient approximation for a first-order consistent approximation. We refer to the corrected form as `div_bc`.

We consider the velocity field,  $\mathbf{u} = \sin(\pi(x + y))(\hat{\mathbf{i}} + \hat{\mathbf{j}})$ . The divergence of the velocity is given by,  $\nabla \cdot \mathbf{u} = 2\pi \cos(\pi(x + y))$ . We evaluate the  $L_1$  error in the approximation using eq. (7). In fig. 9, we plot the  $L_1$  error in the divergence approximation in an UP and PP domain. The uncorrected approximation does not display SOC since the discretization error dominates as we approach higher resolutions. Clearly, the corrected form shows SOC even in the case of a PP domain.

---

<sup>2</sup>In this paper, we report order of convergence by fitting a linear regression line and finding its slope.

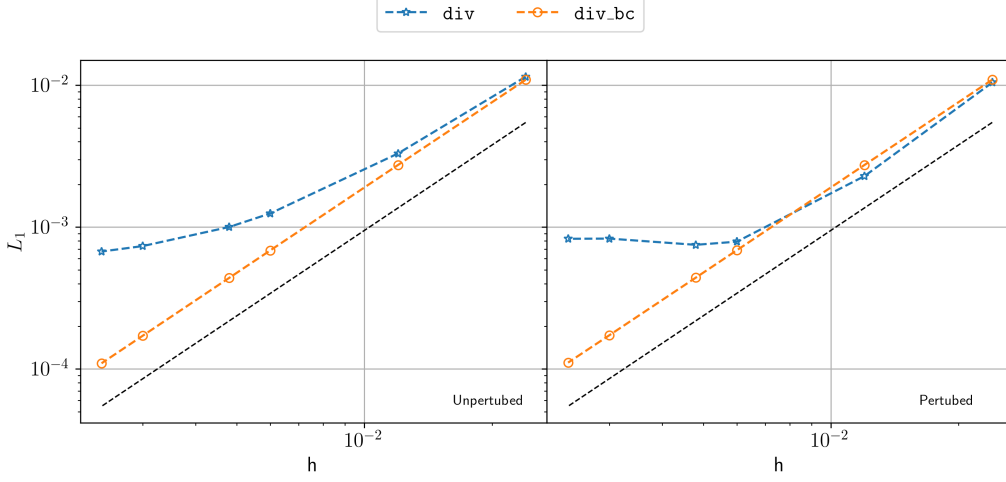


Figure 9: The rate of convergence UP (left) and PP(right) domains for velocity divergence in eq. (11). The dashed line shows the SOC rate. The suffix `_bc` represents the corresponding form with Bonet correction.

In order to evaluate the accuracy of the approximation in a divergence-free field, we consider the velocity field,

$$\begin{aligned} u &= -\cos(2\pi x) \sin(2\pi y), \\ v &= \sin(2\pi x) \cos(2\pi y). \end{aligned} \tag{12}$$

In the fig. 10, we plot the  $L_1$  error using eq. (7) in the divergence computation as a function of resolution for the UP and PP domain. Clearly, the divergence is zero in a UP domain owing to the symmetry of the particles. However, the error in PP domain remains about the same order as seen in the case of general field in fig. 9<sup>3</sup>. Clearly, the Bonet correction does not correct this issue. We observe the implication of this behavior when we compare the schemes in section 5.4.

The continuity equation corresponds to the mass conservation of the system, since mass of each particle is kept constant, we satisfy the global conservation of mass implicitly.



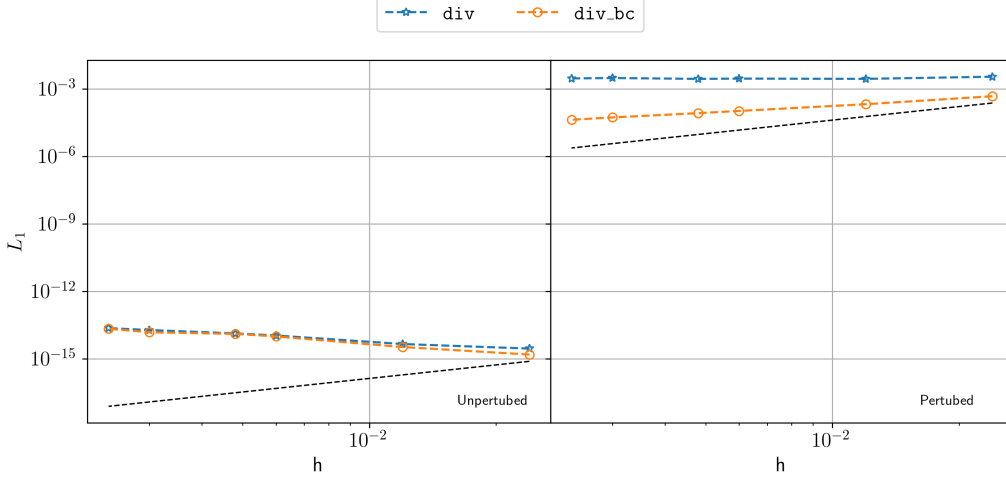


Figure 10: The rate of convergence UP (left) and PP(right) domains for velocity divergence for a divergence-free field. The dashed line shows the SOC rate. The suffix `_bc` represents the corresponding form with Bonet correction.

Name	Expression	Used in
Cleary	$2(\mathbf{u}_i - \mathbf{u}_j) \frac{\nabla W_{ij} \cdot \mathbf{x}_{ij}}{ \mathbf{x}_{ij} ^2} \omega_j$	WCSPH [26, 30]
Fatehi	$2\omega_j \left( \frac{(\mathbf{u}_i - \mathbf{u}_j)}{ \mathbf{x}_{ij} } - \frac{\mathbf{x}_{ij} \cdot (\nabla \mathbf{u})_i}{ \mathbf{x}_{ij} } \right) \frac{\nabla W_{ij} \cdot \mathbf{x}_{ij}}{ \mathbf{x}_{ij} }$	modified WCSPH [27]
tvf	$\frac{1}{m_i} (\omega_i^2 + \omega_j^2) (\mathbf{u}_i - \mathbf{u}_j) \frac{\nabla W_{ij} \cdot \mathbf{x}_{ij}}{ \mathbf{x}_{ij} ^2}$	TVF [13], EDAC [37]
coupled	$((\nabla \mathbf{u})_j - (\nabla \mathbf{u})_i) \cdot \nabla W_{ij} \omega_j$	Bonet and Lok [9]

Table 4: The various approximations of  $\nabla^2 \mathbf{u}$ . The column “expression” is assumed to be summed over the index  $j$  over all the neighbor particles inside the kernel support. The  $\nabla \mathbf{u}_i$  term are calculated using first-order consistent formulation i.e. `asym_bc`

#### 4.3. Comparison of $\nabla^2 \mathbf{u}$ approximation

In this section, we compare various approximations for the Laplacian operator listed in table 4. We refer to the symmetric formulations of [26, 24] as

<sup>3</sup>We discuss the source of this behavior in Appendix B

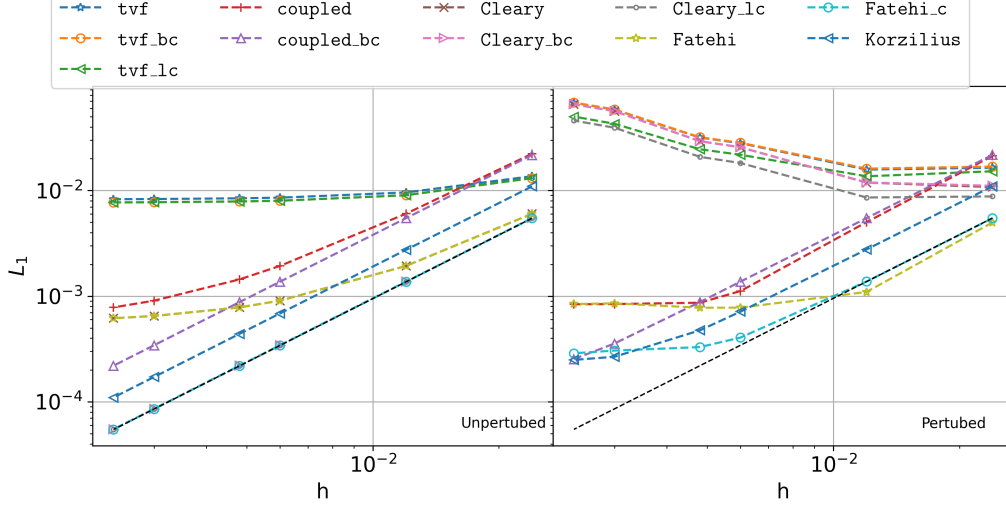


Figure 11: The rate of convergence UP (left) and PP(right) domains for various approximations of the Laplacian operator in table 4. The dashed line shows the SOC rate. The suffixes `_bc` and `_lc` represent the corresponding form with the Bonet correction and Liu correction, respectively. The `Fatehi_c` refers to the `fatehi` formulation with the correction proposed by Fatehi and Manzari [27] (See Appendix C).

Name	$\frac{F_T}{F_{max}}$	$T_r$	$L_1$ error	Order
Cleary_bc	-1.28e+00	1.95	6.55e-02	-0.83
Cleary_lc	-2.15e-01	2.43	4.59e-02	-0.79
Cleary	-1.08e-10	1.12	6.54e-02	-0.84
Fatehi_c	1.69e+00	4.10	2.88e-04	1.30
Fatehi	1.30e+00	2.70	8.43e-04	0.68
Korzilius	1.61e+00	4.66	2.49e-04	1.70
coupled_bc	1.61e+00	3.05	2.54e-04	1.95
coupled	1.30e+00	2.59	8.38e-04	1.46
tvf_bc	-1.26e+00	2.07	6.80e-02	-0.66
tvf_lc	-2.16e-01	2.35	5.01e-02	-0.56
tvf	-1.06e-10	1.00	6.77e-02	-0.67

Table 5: The ratio  $\frac{F_T}{F_{max}}$  showing the total force in the system due to lack of conservation of the approximation and the time taken,  $T_r$  relative to the `tvf` formulation, and  $L_1$  error for  $500 \times 500$  particle case in a PP domain. The last column shows order of convergence for all the methods listed in first column.

**Cleary**, and those of [13] as **tvf**. These ensure that linear momentum is conserved. We also consider the coupled formulation used by [9, 28] and refer to these as **coupled**. This formulation shows oscillations in the approximation when the initial condition is discontinuous. However, to remedy this, one can perform a first-order accurate approximation near the discontinuity and then perform this approximation as shown in [29]. We consider the improved formulation proposed by Fatehi and Manzari [27] referred as **Fatehi**. Both the **coupled** and **Fatehi** formulations are asymmetric. These formulations are performed in two steps where the first step involves computation of velocity gradient for each particle. We also consider the kernel correction applied to each of these formulations. In the case of **Cleary**, **tvf**, and **coupled** methods, we use the standard Bonet and Liu corrections. However, in the case of **Fatehi**, we use the correction tensor proposed by Fatehi and Manzari [27] given by

$$\hat{B}_i^{\eta\mu} = - \left( \sum_j \omega_j \partial^\mu W_{ij} x_{ij}^\eta + \sum_j \omega_j r_{ij}^2 \partial^\theta W_{ij} B_i^{T,\theta\alpha} \sum_j \omega_j e_{ij}^\alpha e_{ij}^\eta \partial^\mu W_{ij} \right)^{-1}, \quad (13)$$

where the subscripts are SPH summation indices and superscripts are in tensor notation<sup>4</sup>. We refer to this corrected formulation as **Fatehi.c**. Additionally, the second derivative can also be obtained by taking the double derivative of the kernel [19, 20, 21]. Therefore, we also consider the method proposed by Korzilius et al. [21] that remedies the deficiencies in earlier approaches where the second derivative was employed. We obtain the second derivative of a scalar field using,

$$\tilde{\nabla}^2 u_i = (\tilde{\Gamma})^{-1} \left( \sum (u_j - u_i) \nabla^2 W_{ij} \omega_j - \mathbf{x}_{ij} \langle \nabla u \rangle_i \nabla^2 W_{ij} \omega_j \right) \quad (14)$$

where  $\tilde{\nabla}^2 = \left[ \frac{\partial^2}{\partial x^2}, \frac{\partial^2}{\partial x \partial y}, \frac{\partial^2}{\partial y^2} \right]^T$  is the operator,  $\nabla^2 W_{ij} = \left[ \frac{\partial^2 W_{ij}}{\partial x^2}, \frac{\partial^2 W_{ij}}{\partial x \partial y}, \frac{\partial^2 W_{ij}}{\partial y^2} \right]^T$ . The gradient  $\langle \nabla u \rangle_i$  is approximated using the **asym\_bc** formulation. The correction  $\tilde{\Gamma}$  is given by

$$\tilde{\Gamma}_i = \sum \frac{1}{2} \nabla^2 W_{ij} \zeta_{ij}^T \omega_j - \sum \nabla^2 W_{ij} x_{ji}^T \omega_j B^{-1} \sum \frac{1}{2} \nabla W_{ij} \zeta_{ij}^T \omega_j \quad (15)$$

---

<sup>4</sup>The term  $*_{ij}$  is widely used in SPH literature and so we use tensor indices in the superscript to derive eq. (13) in Appendix C.

where  $\zeta_{ij} = [x_{ij}^2, x_{ij}y_{ij}, y_{ij}^2]$  and  $B$  is the Bonet correction matrix (see (A.1)). We refer to this formulation as **Korzilius**.

In the fig. 11, we plot the rate of convergence for the various formulations discussed above in both UP and PP domains. In the UP domain, all the methods at least show zeroth-order convergence. All methods without corrections suffer from high discretization error that dominates at higher resolutions [27]. When either Bonet or Liu corrections are employed, **Cleary**, **coupled**, **Fatehi\_c**, and **Korzilius** methods show SOC. The **coupled** method is approximately half an order less accurate as compared to **Cleary** and **Fatehi**. The accuracy of **Korzilius** method is in between the **coupled** and **Fatehi** method. The **tvf** method is very inaccurate as the discretization error increases due to the introduction of  $\omega_i^2 + \omega_j^2$ .

It is important to note that in the PP domain, the symmetric methods diverge due to discretization error of  $O(\frac{\tilde{d}}{h^2} \frac{\Delta s}{h})$ , where  $\tilde{d}$  is the deviation from the regular particle arrangement [27]. Only the **coupled**, **Korzilius**, and **Fatehi** methods show a positive convergence rate. On applying the corresponding correction, the **coupled**, **Korzilius**, and **Fatehi** methods improve. The accuracy for **coupled**, **Korzilius**, **Fatehi** is maintained as observed in the case of UP domain.

In the table 5, we tabulate the total force as a result of the approximation, the time taken for the approximation, and the error on a PP domain consisting of  $500 \times 500$  particles with the order of convergence in the last column for each method plotted in fig. 11. We observe a similar increase in computational time due to the Bonet and Liu corrections as seen in the case of gradient approximation. The **coupled** **Korzilius**, and **Fatehi** formulation have even higher computational cost due to the additional step of velocity gradient computation. The **Korzilius** method requires additional time since the double derivative of the kernel is involved. The **Fatehi\_c** method has an additional step where we compute the second-order tensor in eq. (13) for each particle resulting in a further increase in computation time. We observe a similar increase in total force when an asymmetric version of the formulation is employed, as seen in the case of gradient approximation. Clearly, both the **coupled**, **Korzilius**, and **Fatehi** formulation results in an equal amount of total force resulting in a lack of conservation of linear momentum. In order to get a SOC approximation, we can use either of **coupled\_bc**, **Korzilius**, or **Fatehi\_c** formulations for viscous force estimation.

## 5. Comparison of schemes

In this section, we compare the convergence of several SPH schemes. However, given the results of the previous section, we first propose a SOC scheme using the right combination of discretizations.

### 5.1. A SOC WCSPH scheme

In this section, we discuss a SOC scheme for weakly compressible fluid flows. We consider the fluid density as a property,  $\varrho$  carried by a particle. The numerical density,  $\rho$ , and volume,  $\omega$  are a function of the surrounding particle distribution. The mass,  $m$  of the particle satisfy  $m_i = \varrho_i V_i = \rho_i \omega_i$  where  $V_i$  is the physical volume of the particle occupied by the particle and  $\omega_i$  is the numerical volume used for integration. Thus, we can approximate the fluid density using the standard SPH approximation given by

$$\varrho_i = \sum_j \varrho_j W_{ij} \omega_j. \quad (16)$$

In case of weakly compressible SPH, the requirement of linear momentum conservation condition may be relaxed and is only satisfied approximately [59, 9, 56]. Therefore, we use the SOC approximations that are non-conservative discussed in section 4. In table 6, we list all the discretizations that we can employ to obtain a SOC WCSPH scheme.

Operators	Possible discretization for SOC
Gradient	<code>asym_c</code> , <code>sym1_l</code>
Divergence	<code>div_c</code>
Laplacian	<code>coupled_c</code> , <code>Fatehi_c</code> , <code>Korzilius</code>

Table 6: The operators and their discretization suitable for a SOC scheme.

Furthermore, one can solve the fluid flow equations by assuming the Lagrangian nature as well as the Eulerian nature. We discuss the scheme for both the context in the following sections.

### 5.1.1. Lagrangian method

In the Lagrangian description, the continuity equation and the momentum equation are given by

$$\begin{aligned}\frac{d\rho}{dt} &= -\rho \nabla \cdot \mathbf{u} \\ \frac{d\mathbf{u}}{dt} &= -\frac{\nabla p}{\rho} + \nu \nabla^2 \mathbf{u},\end{aligned}\tag{17}$$

In order to evaluate the RHS of the above equations, one may employ any method listed in table 6. The pressure is evaluated using an equation of state given by

$$p_i = \frac{\rho_o c_o^2}{\gamma} \left( \left( \frac{\rho}{\rho_o} \right)^\gamma - 1 \right),\tag{18}$$

where  $\gamma = 7$ ,  $\rho_o$  is the reference density, and  $c_o$  is the reduced speed of sound. We note that the linear equation of state where in eq. (18),  $\gamma = 1$ , works equally well. We integrate the particles in time using a Runge-Kutta 2<sup>nd</sup> order integrator.

Since we use an asymmetric form of the pressure gradient approximation, particles tend to clump together due to absence of a redistributing background pressure [55]. We use the iterative particle shifting proposed by Huang et al. [12] after every few iterations to redistribute the particles. We compute the shifting vector for the  $m^{\text{th}}$  iteration (of the shifting iterations) using

$$\delta \mathbf{x}_i^m = h_i \sum_j \mathbf{n}_{ij} W_{ij} \omega_j,\tag{19}$$

where  $\mathbf{n}_{ij} = \mathbf{x}_{ij}/|\mathbf{x}_{ij}|$ . The new particle position,

$$\tilde{\mathbf{x}}_i^{m+1} = \mathbf{x}_i^m + \delta \mathbf{x}_i^m\tag{20}$$

is computed. The particles are shifted until the criterion,

$$|\max(\chi^m) - \chi_o| < \epsilon\tag{21}$$

is satisfied up to a maximum of 10 iterations, where  $\chi^m = h^2 \sum_j W_{ij}^m$ ,  $\chi_o$  is the value for uniform distribution, and  $\epsilon$  is an adjustable parameter. In order to keep the approximation of the particle  $O(h^2)$  accurate, we update the particle properties after shifting by,

$$\phi(\tilde{\mathbf{x}}_i) = \phi(\mathbf{x}_i) + (\tilde{\mathbf{x}}_i - \mathbf{x}_i) \cdot \nabla \phi(\mathbf{x}_i),\tag{22}$$

where  $\tilde{\mathbf{x}}_i$  is the final position after iterative shifting,  $\phi$  is the property to be updated, and  $\nabla\phi(\mathbf{x}_i)$  is the gradient of the property on the last position computed with the Bonet correction. In a variation of the above scheme discussed in section 5.4, we observe that usage of non-iterative PST proposed by [42] results in slightly higher errors but still retains its SOC. We refer to the scheme discussed above as L-IPST-C (Lagrangian with iterative PST and `coupled_c` viscosity formulation). Similarly the method using `Fatehi_c` and `Korzilius` formulation are referred as L-IPST-F and L-IPST-K respectively. We note that we only perform the IPST step every 10 timesteps rather than at every timestep.

### 5.1.2. Eulerian method

In the Eulerian description, the continuity equation is written as

$$\frac{\partial \varrho}{\partial t} = -\varrho \nabla \cdot \mathbf{u} - \mathbf{u} \cdot \nabla \varrho. \quad (23)$$

Since the fluid density  $\varrho$  is not same as the particle density  $\rho$  we do not ignore this term, this is unlike what is done by [41]. The momentum equation is written as

$$\frac{\partial \mathbf{u}}{\partial t} = -\frac{\nabla p}{\varrho} + \nu \nabla^2 \mathbf{u} - \mathbf{u} \cdot \nabla \mathbf{u}. \quad (24)$$

We discretize all the terms using SOC operators listed in table 6. We perform time integration using the RK2 integrator; however, we note that the positions of the particles are not updated.

### 5.2. Comparison with other SPH schemes

As discussed in the section 1, many weakly-compressible SPH schemes have been proposed. In this section, we compare the following schemes:

1. TVF : Transport velocity formulation proposed by Adami et al. [13].
2.  $\delta^+$ -SPH : The improved  $\delta$ -SPH formulation proposed by Sun et al. [33].
3. EDAC : Entropically Damped artificial compressibility SPH formulation proposed by Ramachandran and Puri [37].
4. EWCSPH : The Eulerian SPH method proposed by Nasar et al. [41].
5. L-IPST-C : The Lagrangian method with iterative PST and `coupled_c` viscosity formulation discussed in section 5.1.1.

In order to compare these schemes, we consider the Taylor-Green vortex problem. We choose this problem, since it is periodic, has no solid boundaries, and admits an exact solution. The solution of the Taylor-Green problem is given by

$$\begin{aligned} u &= -Ue^{bt} \cos(2\pi x) \sin(2\pi y), \\ v &= Ue^{bt} \sin(2\pi x) \cos(2\pi y), \\ p &= -0.25U^2 e^{2bt} (\cos(4\pi x) + \cos(4\pi y)), \end{aligned} \quad (25)$$

where  $b = -8\pi^2/Re$ , where  $Re$  is the Reynolds number of the flow. We consider  $Re = 100$  and  $U_{max} = 1$ . For the Lagrangian schemes, we consider a perturbed periodic (PP) arrangement of particles shown in the fig. 1 for different resolutions. At  $t = 0$  we initialize the pressure  $p$  and velocity  $(u, v)$  using eq. (25) for all the schemes. Since the fluid density  $\rho$  is a function of pressure, we initialize density inverting eq. (18). In the case of the EWCSPH scheme we consider an unperturbed periodic (UP) arrangement of particles and initialize the  $\rho$  using the prescribed pressure. We compute the  $L_1$  error in pressure and velocity by

$$L_1(h) = \sum_j \sum_i \frac{|f(\mathbf{x}_i, t_j) - f_o(\mathbf{x}_i, t_j)|}{N} \Delta t \quad (26)$$

where,  $h = h_{\Delta s} \Delta s$  is the smoothing length of the kernel,  $\Delta t$  is the timestep,  $N$  is the total number of particles in the domain,  $f$  is either pressure or velocity, and  $f_o$  is the exact value obtained using eq. (25). The particle spacing,  $\Delta s$  is set according to the resolution. We consider resolutions of  $50 \times 50$  to  $500 \times 500$  particles in a  $1m \times 1m$  periodic domain. In order to isolate the effect of spatial approximations on the convergence, we set timestep,  $\Delta t = 0.3h/(U_{max} + c_o)$ , where  $h = 1.2/500$  is set corresponding to highest resolution,  $c_o = 10U_{max}$ , for all the simulations. We run all the simulations for 1 timestep and observe convergence. We choose one timestep since most of the scheme considered diverge.

In the fig. 12, we plot the  $L_1$  error evaluated using eq. (26) for pressure and velocity in the domain for different schemes. Clearly, none of the schemes show convergence in pressure. It is because the initial velocity is divergence-free, so there is no change in density and thereby pressure. We observe that the EDAC, EWCSPH, and L-IPST-C schemes are almost four orders more accurate than the TVF and  $\delta^+$ SPH schemes. In case of both the TVF and



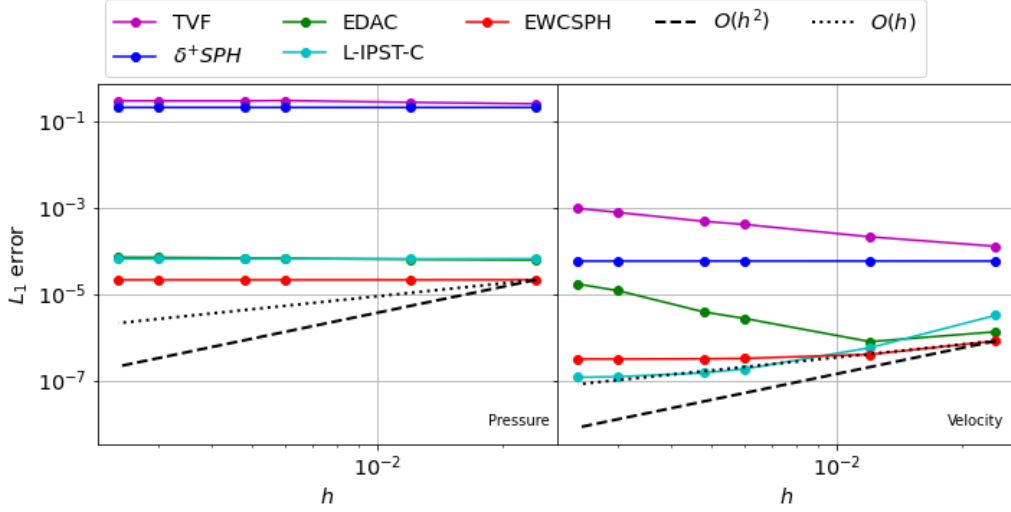


Figure 12: Convergence of  $L_1$  error in pressure (left) and velocity (right) with the change in resolution. The  $Re = 100$ ,  $c_o = 10$ ,  $\Delta t = 6.54 \times 10^{-5}$  and only 1 timestep taken.

$\delta^+$ SPH schemes, we link the pressure with particle density  $\rho$ , which is a function of the particle configuration. The particle positions are a result of the particle shifting, and therefore, the pressure is incorrectly captured. On the other hand, the other schemes either use a pressure evolution equation (EDAC) or a fluid density to evaluate pressure. In the case of the EWCSPH scheme, we initialize density using the pressure values in the eq. (18) which results in better accuracy.

The  $L_1$  error in velocity diverges in the case of the TVF and EDAC schemes since these use a symmetric form of type **sym2** in table 2 to discretize

Name	$\frac{F_T}{F_{max}}$	$T_r$	$L_1( \mathbf{u} )(O)$	$L_1(p)(O)$
$\delta^+SPH$	2.19e-05	1.49	5.69e-05(0.00)	2.03e-01(0.00)
EDAC	1.88e-07	1.32	1.68e-05(-1.24)	7.00e-05(-0.07)
EWCSPH	7.03e-15	2.25	3.13e-07(0.38)	2.10e-05(0.00)
L-IPST-C	1.34e-05	3.36	1.18e-07(1.42)	6.41e-05(0.00)
TVF	3.70e-16	1.00	9.45e-04(-0.88)	2.88e-01(-0.07)

Table 7: Table showing total force w.r.t. the maximum force in the domain and the time taken for 1 iteration w.r.t. the TVF scheme for all the schemes.

the momentum equation. Whereas, in the case of the  $\delta^+$ SPH scheme, `sym1` type of discretization is employed leading to less errors. Moreover, the  $\delta^+$ SPH scheme uses a consistent formulation and both TVF and EDAC schemes are inconsistent when the shifting (transport) velocity is added to the momentum equation [33]. The EWCSPH, and L-IPST-C formulations show convergence (not second-order) as expected. We observe that in the velocity convergence a constant leading error term dominates resulting in flattening at higher resolutions. Since, we use second-order accurate formulations in L-IPST-C and EWCSPH<sup>5</sup> formulations, the only equation which is not converging with resolution is the equation of state (EOS).

In this section, we focus on highlighting the effect of using fluid density  $\varrho$  different than the numerical density  $\rho$ . It allows a better convergence rate and independence of density from particle positions. In contrast to this, the use of numerical density as a function of particle position is consistent with the volume used for the SPH approximation. In TVF,  $\delta^+$ -SPH, EDAC and, EWCSPH schemes, we make no such distinction, and use the fluid density  $\rho$  in the numerical volume  $\omega_j = m_j/\rho_j$ . The poor convergence for these schemes show that it is important to treat the fluid and numerical densities differently.

In the table 7, we tabulate the total force and the time taken by the scheme for one timestep with the errors and order of convergence in pressure and velocity for the  $500 \times 500$  resolution case. It is clear that the TVF and EWCSPH schemes conserve linear momentum and take the least amount of time. The EDAC and the  $\delta^+$ -SPH scheme do not conserve linear momentum exactly. In the case of the EDAC scheme the use of average pressure in the pressure gradient evaluation results in lack of conservation. Whereas, in the case of  $\delta^+$ -SPH the asymmetry of the shifting velocity divergence causes lack of conservation. The L-IPST-C scheme is known to be non-conservative; however, the value is comparable to other schemes. The time taken by the L-IPST-C scheme is significantly higher due to the evaluation of correction matrices.

### 5.3. The effect of $c_o$

In the schemes discussed in the previous section, except the EDAC scheme<sup>6</sup>, we impose artificial compressibility (AC) using the EOS, which is  $O(M^2)$

---

<sup>5</sup>It is second-order accurate since a uniform stationary grid is used.

<sup>6</sup>The EDAC scheme uses a pressure evolution equation.

accurate [60, 38], where  $M = U_{max}/c_o$  is the Mach number of the flow. Chorin [60] originally proposed this method to obtain steady-state solutions of an incompressible flow. Some authors have used artificial compressibility with dual-time stepping to achieve truly incompressible time-accurate results [61, 62]. We achieve the incompressibility limit when  $c_o \rightarrow \infty$ .

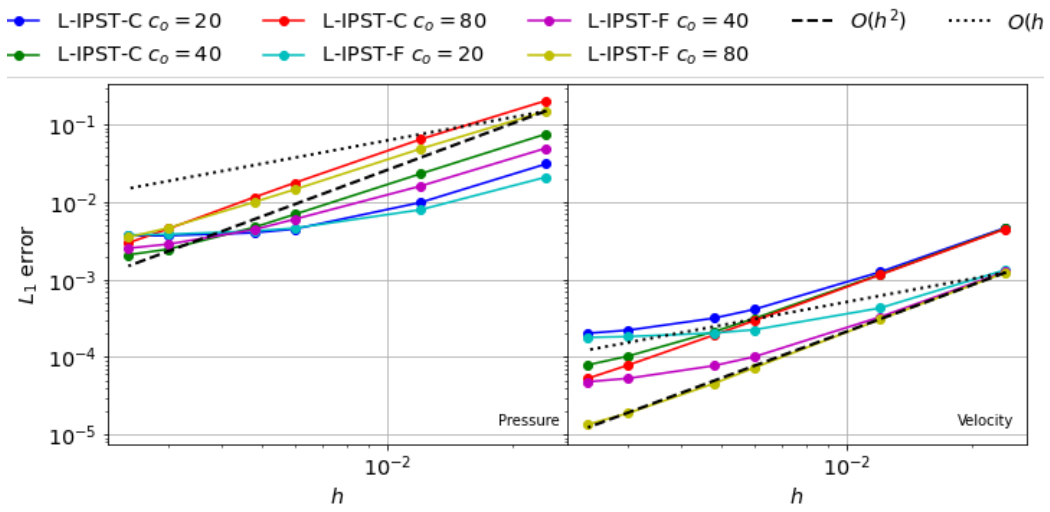


Figure 13: Convergence rates for pressure (left) and velocity (right). The L-IPST-C and L-IPST-F methods are compared for different values of  $c_o$ .

Name	$\frac{F_T}{F_{max}}$	$T_r$	$L_1( \mathbf{u} )(O)$	$L_1(p)(O)$
L-IPST-C $c_o = 20$	7.13e-05	1.00	2.03e-04(1.38)	3.66e-03(0.93)
L-IPST-C $c_o = 40$	9.31e-05	2.15	7.94e-05(1.78)	2.09e-03(1.60)
L-IPST-C $c_o = 80$	1.44e-04	3.76	5.32e-05(1.93)	2.98e-03(1.85)
L-IPST-F $c_o = 20$	7.11e-05	1.23	1.80e-04(0.85)	3.77e-03(0.73)
L-IPST-F $c_o = 40$	5.99e-05	2.84	4.81e-05(1.44)	2.54e-03(1.31)
L-IPST-F $c_o = 80$	1.66e-04	5.46	1.36e-05(1.98)	3.52e-03(1.65)

Table 8: Comparison of total force, time taken relative to the L-IPST-C with  $c_o = 20$ ,  $L_1$  error in velocity and order for different values of  $c_o$ .

This section compares the convergence of the L-IPST-F and L-IPST-C scheme with change in AC parameter i.e. the speed of sound  $c_o$ . We consider the Taylor-Green problem; however, we run the simulation for  $t = 0.5s$ .

In fig. 13, we plot the  $L_1$  error in the pressure and velocity for both the schemes and different  $c_o$ . We observe that both L-IPST-C and L-IPST-F methods are affected by the change in  $c_o$  value significantly as expected. In case of pressure, with the increase in the  $c_o$  value, the error in the lower resolutions increases; however, for higher resolution it improves. Clearly, we attain the increase in the order of convergence in case of the pressure due to increased error scales at lower resolutions. The increase in error is attributed to the inability of the SPH operators to correctly capture a divergence free velocity field as discussed in section 4.2. However, on looking at the velocity convergence, both the schemes attain SOC even at higher resolutions. We observe, though, at lower resolutions, the error in the pressure increases with the  $c_o$  value. As observed in the case of the Laplace operator comparison in section 4.3, the use of `Fatehi_c` discretization offers better accuracy.

In the table 8, we tabulate the total force, relative time, and the  $L_1$  error in pressure and velocity with the order of convergence for  $500 \times 500$  particles. We observe that at a higher  $c_o$  value, the total force is less compared to the simulation when  $c_o$  values are lower. From the table, we can see that the use of L-IPST-F scheme offers better accuracy at the cost of the extra time taken. We also note that one can choose to use lower values of  $c_o$  at lower resolutions and increase the value as the resolution increase to get better accuracy in pressure. Doing this does not affect the convergence in velocity.

#### 5.4. Study of other SOC variants

In this section, we show that the scheme presented in the section 5.1.1 (L-IPST-C) can be easily converted into other forms for improved accuracy and ease of calculation. We note that regardless of the set of governing equations employed, the discretizations from table 6 must be used to achieve SOC.

In order to remove high frequency oscillations, one could modify the continuity equation given by,

$$\frac{d\rho}{dt} = -\rho \nabla \cdot \mathbf{u} + D \nabla^2 \rho \quad (27)$$

where,  $D = \delta h c_o^2$  is the damping constant, where  $\delta = 0.1$ . This corresponds to the  $\delta$ -SPH scheme [36]. In this case we also use the linear equation of state to evaluate  $p$  given by

$$p = c_o^2(\rho - \rho_o). \quad (28)$$

The following are different variations of the basic scheme:

1. Using different PST : One could use either IPST proposed by [12] or the non-iterative PST proposed by [33]. The properties like  $u, v, p$ , and  $\varrho$  need to be updated using first order Taylor expansions given by

$$\phi(\tilde{\mathbf{x}}_i) = \phi(\mathbf{x}_i) + (\tilde{\mathbf{x}}_i - \mathbf{x}_i) \cdot \nabla \phi(\mathbf{x}_i) \quad (29)$$

where  $\phi$  is the desired property. We use the coupled formulation for the viscosity and non-iterative PST. We refer to this method as L-PST-C.

2. Using pressure evolution: On taking the derivative of EOS in eq. (28) w.r.t. time and using the eq. (27), we get the pressure evolution equation given by

$$\frac{dp}{dt} = -\varrho c_o^2 \nabla \cdot \mathbf{u} + D \nabla^2 p. \quad (30)$$

This is very similar to the EDAC pressure evolution equation[37]. The value of  $\varrho$  can be evaluated from the EOS in eq. (28) given by

$$\varrho = \frac{p}{c_o^2} + \varrho_o. \quad (31)$$

We employ the coupled formulation for viscosity and use IPST for regularization. We refer to this method as PE-IPST-C.

3. Using remeshing for regularization: The regularization step performed using PST in the L-IPST-C method can be replaced with the remeshing procedure of Hieber and Koumoutsakos [40]. The remeshing is performed using the  $M_4$  kernel given by,

$$M_4(q) = \begin{cases} 1 - \frac{5q^2}{2} + \frac{3q^3}{2} & 0 \leq q < 1, \\ \frac{(1-q)(2-q)^2}{2} & 1 \leq q < 2, \\ 0 & q \geq 2, \end{cases} \quad (32)$$

where  $q = |\mathbf{x}|/\Delta s$ , where  $\Delta s$  is the initial particle spacing. The properties on the regular grid are computed using

$$\phi(\tilde{\mathbf{x}}_i) = \frac{\sum \phi(\mathbf{x}_j) M_4(|\tilde{\mathbf{x}}_i - \mathbf{x}_j|, h)}{\sum M_4(|\tilde{\mathbf{x}}_i - \mathbf{x}_j|, h)}, \quad (33)$$

where  $\tilde{\mathbf{x}}$  are points on a regular Cartesian mesh. The remeshing procedure can be performed every few steps; however, we perform remeshing after every timestep. We use the coupled formulation for viscosity. We refer to this method as L-RR-C.

4. Including regularization in the form of shifting velocity: the methods of [13, 34, 33] use shifting by perturbing the velocity of the particles and adding corrections to the momentum equation. Thus the particles are advected using the transport velocity,  $\tilde{\mathbf{u}} = \mathbf{u} + \delta\mathbf{u}$  and the displacement is given by,

$$\mathbf{x}_i^{n+1} = \mathbf{x}_i^n + \Delta t(\mathbf{u}_i + \delta\mathbf{u}_i). \quad (34)$$

The new continuity and momentum equations are given by

$$\begin{aligned} \frac{\tilde{d}\varrho}{dt} &= -\varrho \nabla \cdot \mathbf{u} + D\nabla^2 \varrho + \delta\mathbf{u} \cdot \nabla \varrho, \\ \frac{\tilde{d}\mathbf{u}}{dt} &= -\frac{\nabla p}{\varrho} + \nu \nabla^2 \mathbf{u} + \delta\mathbf{u} \cdot \nabla \mathbf{u}, \end{aligned} \quad (35)$$

where  $\frac{\tilde{d}(\cdot)}{dt} = \frac{\partial(\cdot)}{\partial t} + \tilde{\mathbf{u}} \cdot \nabla(\cdot)$ . In this method, we employ SOC approximations mentioned in table 6. We use the PST proposed in [33] for this scheme along with the coupled formulation for viscosity. We refer to this method as TV-C.

5. Eulerian method: The Eulerian method solves the equation of motion on a stationary grid. This can be derived using the TV-C method by setting  $\delta\mathbf{u}_i = -\mathbf{u}_i$ . This substitution makes the transport velocity in the eq. (34) equal to zero, thus the particle does not move. The modified equation on setting  $\delta\mathbf{u}_i = -\mathbf{u}_i$  in eq. (35), we get

$$\begin{aligned} \frac{\partial \varrho}{\partial t} &= -\varrho \nabla \cdot \mathbf{u} + D\nabla^2 \varrho - \mathbf{u} \cdot \nabla \varrho, \\ \frac{\partial \mathbf{u}}{\partial t} &= -\frac{\nabla p}{\varrho} + \nu \nabla^2 \mathbf{u} - \mathbf{u} \cdot \nabla \mathbf{u}. \end{aligned} \quad (36)$$

Therefore, we recover the governing equation for the Eulerian method. We note that unlike [41], we retain the last term in the continuity equation. We use the coupled formulation to discretize viscous term. We refer to this method as E-C (Eulerian method with `coupled_c` viscosity formulation) method.

We simulate the Taylor-Green problem using  $c_o = 80$  for a duration of 0.5s with different resolutions. In addition, we study the performance of the EWCSPH scheme since it is computationally efficient and accurate. In the fig. 14, we plot the error in pressure and velocity for all the schemes. In the

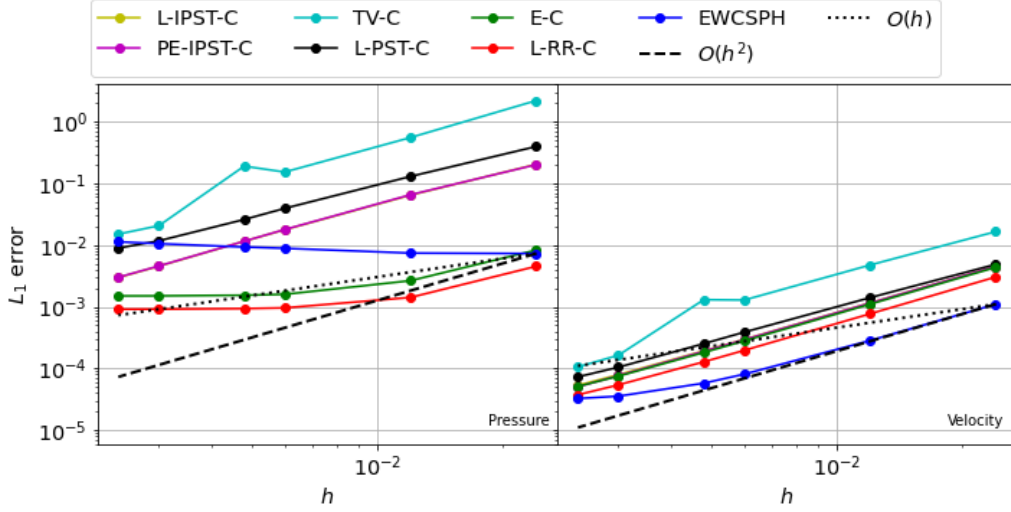


Figure 14: Convergence rates for pressure (left) and velocity (right) of different variants of SOC schemes.

table 9, we tabulate the total force, relative time,  $L_1$  error in pressure and velocity at  $500 \times 500$  resolution, and the order of convergence.

The L-IPST-C and PE-IPST-C overlap in both the pressure and velocity convergence plots, and these are both approximately second-order. Compared to L-IPST-C, the L-PST-C shows lower convergence rate, and TV-C shows higher order of convergence, whereas E-C and L-RR-C show very poor convergence rates in pressure; however, the L-RR-C method shows very low errors in pressure. The EWCSPH has a negative convergence rate in pressure. While the TV-C shows a high convergence rate, it has much larger errors than all the other schemes considered for both pressure and velocity. The E-C, L-IPST-C, L-RR-C, and PE-IPST-C show high convergence rates in velocity as expected. The L-PST-C shows slightly high error and 1.84 convergence rate. The EWCSPH shows a lower convergence rate of 1.57 but is the most accurate of all the schemes regarding the velocity error.

The TV-C scheme shows low accuracy since we perform the shifting using an additional term in the momentum equation compared to the PE-IPST-C and L-IPST-C. This decrease in accuracy is also visible in the case of velocity. The L-PST-C scheme show higher error suggesting that the non-iterative PST does not perform the required amount of regularization. Both L-RR-C and E-C are comparable and most accurate. These schemes have lower

Name	$\frac{F_T}{F_{max}}$	$T_r$	$L_1( \mathbf{u} )(O)$	$L_1(p)(O)$
E-C	8.13e-15	1.19	5.11e-05(1.94)	1.50e-03(0.71)
EWCSPPH	1.07e-14	1.00	3.25e-05(1.57)	1.13e-02(-0.20)
L-IPST-C	1.44e-04	1.53	5.32e-05(1.93)	2.98e-03(1.85)
L-PST-C	2.64e-06	2.02	7.31e-05(1.84)	8.93e-03(1.68)
L-RR-C	1.51e-18	1.41	3.74e-05(1.92)	9.11e-04(0.65)
PE-IPST-C	6.17e-05	1.65	5.05e-05(1.96)	3.01e-03(1.84)
TV-C	-5.01e-06	1.88	1.06e-04(2.18)	1.51e-02(2.14)

Table 9: Comparison of total force, time taken relative to L-IPST-C with  $c_o = 20$ ,  $L_1$  error in velocity and pressure for variation of schemes with  $c_o = 80$ .

error since the particles are fixed on a cartesian grid resulting in accurate computation of divergence as discussed in section 4.2. The pressure convergence flattens since it reaches the limit of accuracy possible with this value of  $c_o = 80$  and further accuracy may be seen by increasing this further.

Clearly, the total force in case of E-C, L-RR-C, and EWCSPPH scheme is zero since we compute the acceleration on a uniform Cartesian grid of particles. However, the total force in other schemes are accurate to order  $10^{-5}$ . The times taken shows that L-PST-C is the highest since we apply the PST at every timestep, the TV-C involves many terms in the equations and therefore takes a lot of time. The E-C, and EWCSPPH take the least time since they do not use a PST <sup>7</sup>. The L-RR-C, L-IPST-C, and PE-IPST-C take a similar amount of time.

### 5.5. Conservation of SOC schemes

Thus far we, have looked at the convergence of the various schemes. In this section, we look at the schemes listed in table 9 from the perspective of conservation of linear and angular momentum.

<sup>7</sup>These methods can be made even faster since the neighbors need not be updated, and the correction matrices can also be computed once and saved.



### 5.5.1. The Gresho vortex

We consider the Gresho vortex problem [45], which is an inviscid incompressible flow problem having the pressure and velocity fields given by,

$$p(r), u_\phi(r) = \begin{cases} 12.5r^2 + 5, 5r & 0 \leq r < 0.2, \\ 12.5r^2 - 20r + 4 \ln(5r) + 9, 2 - 5r & 0.2 \leq r < 0.4 \\ 3 + 4 \ln(2), 0 & 0.4 \leq r \end{cases} \quad (37)$$

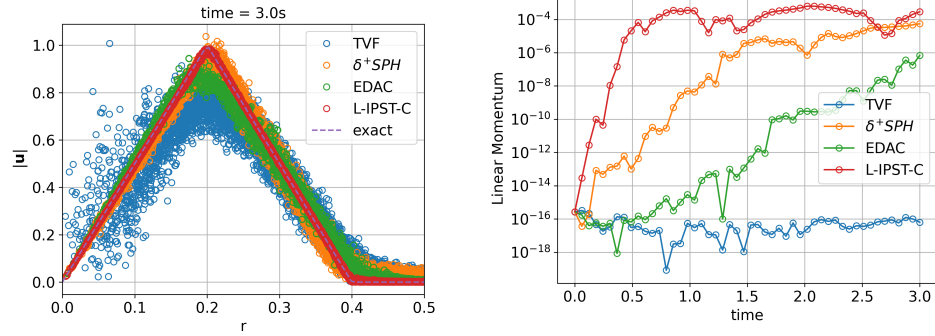


Figure 15: The velocity of particles with the distance from the center of the vortex (left) and the  $x$ -component of the total linear momentum (right) for all the schemes.

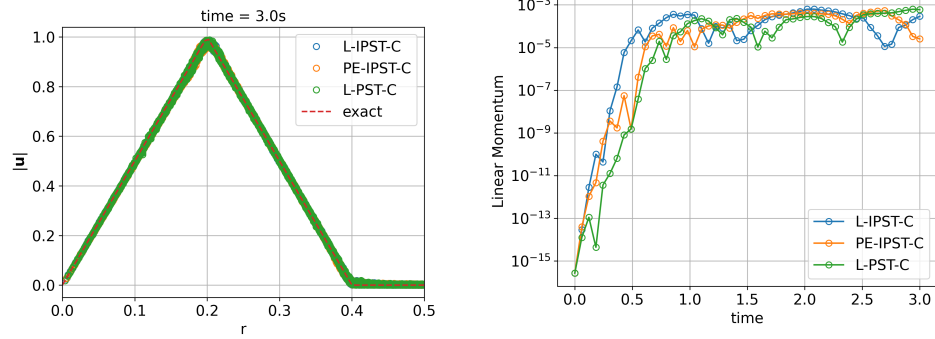


Figure 16: The velocity of particles with the distance from the center of the vortex (left) and the the  $x$ -component of the total linear momentum (right) for the variation of SOC scheme.

We consider an unperturbed periodic domain of size  $1 \times 1$  with the center at  $(0,0)$ . We set the kinematic viscosity,  $\nu = 0$ , and the time step and other

properties as done in the Taylor-Green problem. The problem is simulated until  $t = 3s$ . Since the problem is inviscid, we expect the scheme to retain the velocity and pressure field. We do not use artificial viscosity in the simulations for any of the schemes. We perform the simulation of all the schemes listed in table 7 except the EWCSPH scheme<sup>8</sup>. We note that using an initial perturbed particle configuration results in very diffused results for all schemes except the L-IPST-C.

In the fig. 15, we plot the velocity of the particles with the distance,  $r$  from the center (on left) and the  $x$ -component of the total linear momentum with time for a  $100 \times 100$  particle simulation. The L-IPST-C scheme retains the velocity profile very well. The  $\delta^+$ -SPH, EDAC, and TVF schemes show diffusion due to inaccuracy in the pressure gradient evaluation. Except for the TVF scheme, the rest show a finite increase in the momentum bounded at  $10^{-4}$ . Clearly, approximate linear momentum conservation is sufficient to obtain accurate results in the case of weakly compressible flows.

We also perform the simulations with different versions of the SOC scheme listed in table 9<sup>9</sup>. In the fig. 16, we plot the velocity with the distance from the center and the  $x$ -component of the linear momentum with time for  $100 \times 100$  particle simulation. Clearly, all the schemes are accurate and approximately conserve linear momentum as expected.

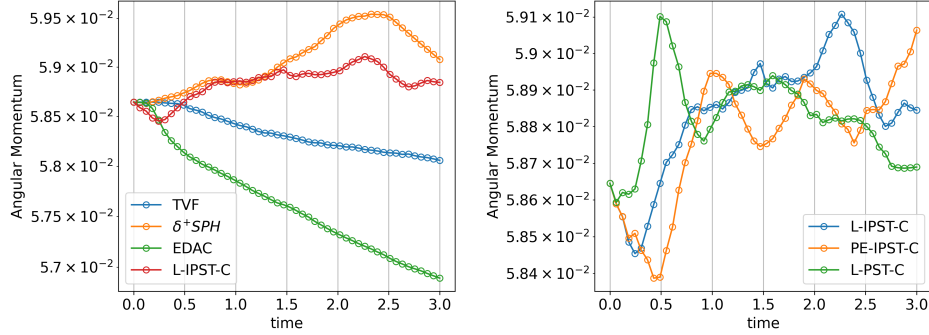


Figure 17: The angular momentum variation with time for Gresho-Chan vortex for different schemes.

In fig. 17, we show the angular momentum variation with time for different

<sup>8</sup>We discuss The failed simulations are discussed in the Appendix E.

<sup>9</sup>The L-RR-C, TV-C, and E-C scheme fail to complete the simulation, and these are discussed in the Appendix E

schemes. None of the schemes conserve angular momentum, but for the SOC schemes, the variations are very small and  $O(5 \times 10^{-4})$ .

### 5.5.2. The incompressible shear layer

The incompressible shear layer simulates the Kelvin-Helmholtz instability in an incompressible flow. This test case produces non-physical vortices for the schemes where the operators are under resolved even when the scheme is convergent [46]. The initial condition for the velocity in x direction is given by

$$u = \begin{cases} \tanh(\rho(y - 0.25)) & y \leq 0.5, \\ \tanh(\rho(0.75 - y)) & y > 0.5, \end{cases} \quad (38)$$

where  $\rho = 30$ . In order to begin the instability, a small velocity is given in y direction,

$$v = \delta \sin(2\pi x), \quad (39)$$

where  $\delta = 0.05$ . We consider a small viscosity  $\nu = 1/10000$ . We simulate the problem using all the schemes listed in table 7. In fig. 18 and fig. 19, we plot the vorticity field for the schemes<sup>10</sup> discussed in this paper. We note that unlike the inviscid problem of Gresho-Chan vortex, the scheme EWCSPH, TV-C and E-C shows results matching other SOC schemes. In fig. 18, we observe that TVF scheme and  $\delta^+$ -SPH scheme show high frequency oscillations and while the EDAC scheme is much better; However, it shows some undesired artifacts.

## 6. Cost of computation

In this section, we compare the cost of computation of all the schemes considered in this study. We simulate the Taylor-Green problem for 5000 timesteps with 50, 100, and 200 resolutions for all the schemes. We use Intel(R) Xeon(R) CPU E5-2650 v3 processor and ran all the simulations in serial. In fig. 20, we plot the  $L_1$  error in velocity computed using the eq. (26) as a function of time taken for the simulation. Clearly, all the SOC schemes are close to each other in terms of errors. The E-C and EWCSPH scheme takes very less time and are very accurate; however, EWCSPH is not

---

<sup>10</sup>The L-RR-C method failed to run due to discontinuity in the initial velocity field.

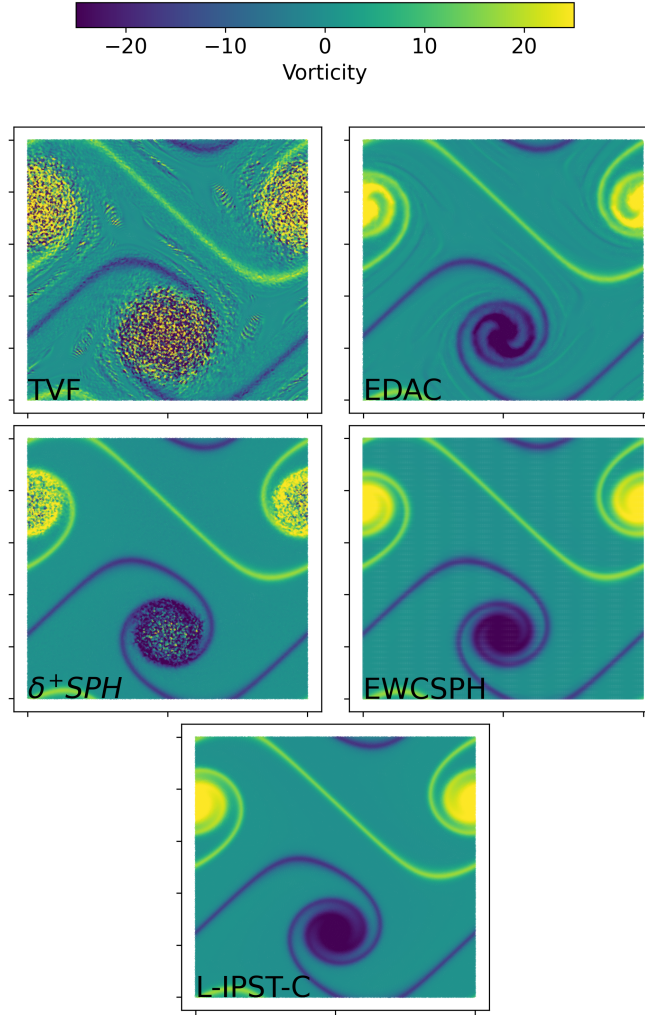


Figure 18: Vorticity contour plot for  $500 \times 500$  resolution for all the schemes.

convergent in pressure as shown in section 5.2. The EDAC scheme has lower error comparable to the SOC schemes; however, its convergence rate reduces

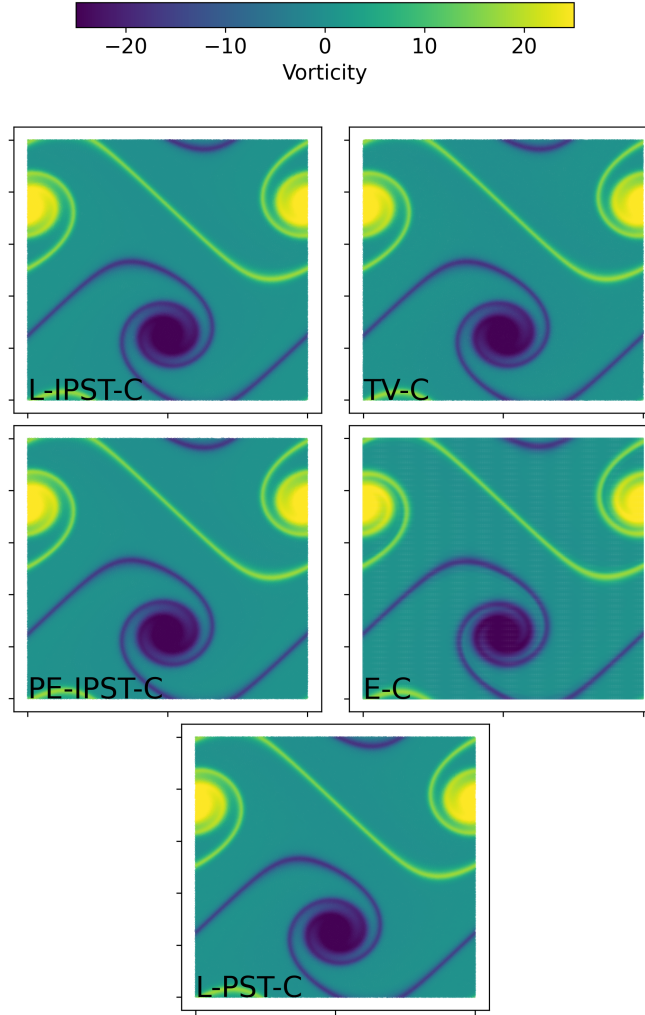


Figure 19: Vorticity contour plot for  $500 \times 500$  resolution for all the schemes.

with increase in resolution. We show that despite having higher time taken by the SOC schemes, they achieve higher accuracy with a fewer number of

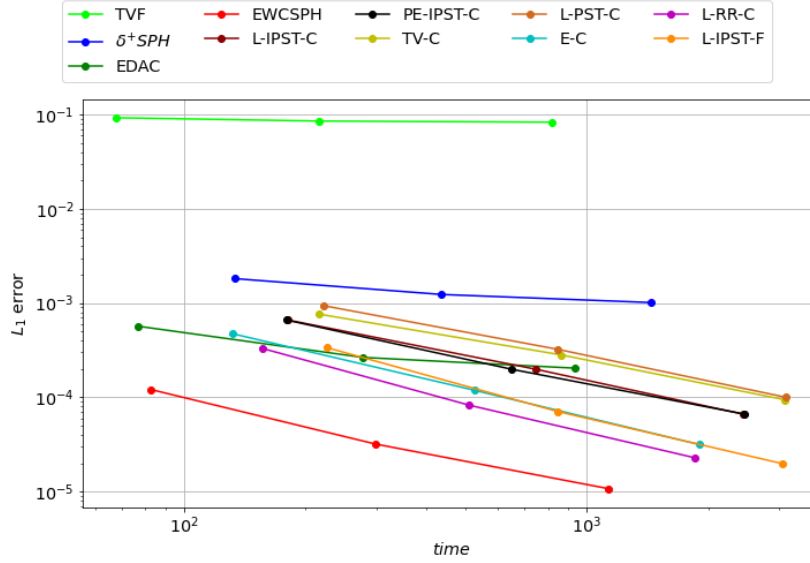


Figure 20: The  $L_1$  error in velocity with respect to the time taken to evaluate 5000 timesteps for all the schemes discussed in the previous sections.

particle also, for some schemes, these accuracy levels are not achievable at all.

We implement the schemes using the open source PySPH [63] framework and automate the generation of all the figures presented in this manuscript using the `automan` framework [47]. The source code is available at [https://gitlab.com/pypr/convergence\\_sph](https://gitlab.com/pypr/convergence_sph).

## 7. Discussions and Conclusions

In this paper, we have performed a numerical study of the accuracy and convergence of a variety of SPH schemes in the context of weakly-compressible fluids. Based on the numerical study performed in the previous sections, we summarize the key findings below.

### 7.1. Choice of smoothing kernel

We first considered the SPH approximation of a function and its derivative using different kernels. All the kernels considered here show second-order convergence when the support radius is high. The accuracy is marginally

effected by the change in type of kernel. The smoothing error of an SPH approximation scales as  $O(h^2)$  and this necessitates that the smoothing length of the kernel be as small as possible. This implies that  $h_{\Delta s}$  be small. As is well known, the discretization errors scale as  $O((\frac{\Delta s}{h})^{\beta+2})$  and this necessitates that the smoothing radius be larger. These two requirements are contradictory. We find that by using a modest  $h = 1.2\Delta s$ , along with the kernel corrections of Bonet and Lok [9] or Liu and Liu [10] we are able to obtain close to second-order convergence for the kernels considered in this work. It holds up to a resolution of  $L/\Delta s = 500$ , where  $l = 1m$  which appears to be among the highest resolutions we have seen in the literature concerning the convergence of SPH methods. In the literature, we find kernels like the cubic spline to demonstrate pairing instabilities [44]. We can avoid this instability by using a particle shifting technique (PST).

### *7.2. Choice of suitable operators*

The SPH approximation of operators like the gradient, divergence, and Laplacian must be chosen carefully. In this paper, we recommend two methods for gradient approximation and three methods for viscous term approximation that ensure second-order convergence. The approximations which ensure pair-wise linear momentum conservation are always divergent. In the future, one could explore pair-wise linear momentum conserving and second-order convergent SPH approximation in a perturbed domain using SPH. Furthermore, the widely used artificial compressibility assumption makes the scheme  $O(M^2)$  accurate. We recommend using high  $c_o$  values or a dual-time stepping criteria to achieve convergence. Solving the pressure using the pressure Poisson equation may also provide SOC, although those have not been studied in this work.

### *7.3. Particle density and fluid density*

We recommend that one employ the fluid density in the governing differential equation as a property that convects with the particle. The approximation of the SPH operators should not be a function of a property of the fluid i.e. density. We obtain the integration volume by eq. (5) where the mass and kernel support radius of particles is kept constant. In the future, it would be important to explore the convergence of SPH operators when the mass as well as the support radius of the particles are varying as required by an adaptive SPH algorithm.

#### 7.4. *New scheme and variations*

We demonstrate Eulerian as well as Lagrangian SPH schemes that are second-order convergent. We show that the Eulerian schemes captures the divergence accurately due to symmetry in the particle distribution resulting in better accuracy in pressure. We derive a pressure evolution equation using the continuity equation that resembles the EDAC SPH scheme in literature. We show that the PST step in the Lagrangian method can be replaced by a remeshing step which is another moment conserving regularization. However, remeshing is not stable in the presence of jumps in the properties as observed in the case of the Gresho vortex (See Appendix E) and incompressible shear layer. The PST step can be included in the momentum equation resulting in the  $\delta^+$ -SPH scheme. From the  $\delta^+$ -SPH method, one can obtain the Eulerian form of WCSPH method by setting the shifting velocity to  $-\mathbf{u}$ . All these schemes are SOC when we use a second-order convergent approximation for the operators. We show that even though the schemes are non-conservative in the absolute sense, approximate conservation also produce accurate results in the case of incompressible flows.

Thus, by a judicious choice of discretization, particle shifting, and a separation of the fluid and particle densities we have shown that second-order convergence is possible using the SPH method for weakly-compressible flows. We do observe that the SPH discretization of the divergence operator introduces errors for divergence-free fields which are noticeably absent in the case of an Eulerian method due to the symmetry of the particle distribution. This introduces significant errors into the pressure; it would be valuable to develop more accurate divergence operators for the Lagrangian case.

Given that the proposed schemes are second-order, it would be important to study the boundary conditions employed in the SPH to see how they affect the accuracy and order of convergence. In the future a similar analysis in the context of variable smoothing length, and mass would be very useful in light of many recent developments of an adaptive SPH method. One concern of note is the increased computational effort required to maintain second-order convergence and future developments in this area would be important for practical simulation using the SPH method.



## Appendix A. The kernel corrections

We obtain the kernel correction by Bonet and Lok [9] such that the new kernel,  $\nabla \tilde{W}_{ij} = B_i \nabla W_{ij}$  satisfies,

$$\begin{aligned}
& \sum_j (\mathbf{x}_j - \mathbf{x}_i) \otimes \nabla \tilde{W}_{ij} \omega_j = 1 \\
\Rightarrow & \sum_j (\mathbf{x}_j - \mathbf{x}_i) \otimes B_i \nabla W_{ij} \omega_j = 1 \\
\Rightarrow & B_i = \left( \sum_j \nabla W_{ij} \otimes (\mathbf{x}_j - \mathbf{x}_i) \omega_j \right)^{-1},
\end{aligned} \tag{A.1}$$

where  $B_i$  is the correction matrix for the kernel gradient,  $\nabla W_{ij}$ . The eq. (A.1) represents the first moment of the kernel gradient tends to unity as  $h \rightarrow 0$ . The first order Taylor series of a function,  $f$  defined at  $x$  about  $x_i$  is,

$$f(\mathbf{x}) = f(\mathbf{x}_i) + (\mathbf{x} - \mathbf{x}_i) \cdot \nabla f(\mathbf{x}_i) \tag{A.2}$$

integrating both sides with  $\nabla W$

$$\begin{aligned}
\int f(\mathbf{x}) \nabla W d\mathbf{x} &= \int f(\mathbf{x}_i) \nabla W d\mathbf{x} + \int (\mathbf{x} - \mathbf{x}_i) \cdot \nabla f(\mathbf{x}_i) \nabla W d\mathbf{x} \\
&= \int f(\mathbf{x}_i) \nabla W d\mathbf{x} + \int (\nabla W \otimes (\mathbf{x} - \mathbf{x}_i)) \nabla f(\mathbf{x}_i) d\mathbf{x}.
\end{aligned} \tag{A.3}$$

Using the SPH approximation of the integral on both the sides, we get

$$\begin{aligned}
\sum_i f_j \nabla W_{ij} \omega_j &= \sum_i f_i \nabla W_{ij} \omega_j + \sum_j \nabla W_{ij} \otimes (\mathbf{x}_j - \mathbf{x}_i) \nabla f(x_i) \omega_j \\
\Rightarrow \nabla f(x_i) &= \sum_i (f_j - f_i) B_i \nabla W_{ij} \omega_j.
\end{aligned} \tag{A.4}$$

The eq. (A.4) is  $O(h^2)$  accurate [27]. Therefore, the kernel gradient correction by Bonet and Lok [9] imply the use of **asym** form of the gradient approximation for an  $O(h^2)$  accurate approximation. On the other hand, the correction proposed by Liu and Liu [10], originates by convolving the Taylor series by

$W$  and  $\nabla W$ , and solving all the equation simultaneously. The matrix form is given by

$$\begin{bmatrix} W_{kl}V_l & x_{lk}W_{kl}V_l & y_{lk}W_{kl}V_l & z_{lk}W_{kl}V_l \\ W_{kl,x}V_l & x_{lk}W_{kl,x}V_l & y_{lk}W_{kl,x}V_l & z_{lk}W_{kl,x}V_l \\ W_{kl,y}V_l & x_{lk}W_{kl,y}V_l & y_{lk}W_{kl,y}V_l & z_{lk}W_{kl,y}V_l \\ W_{kl,z}V_l & x_{lk}W_{kl,z}V_l & y_{lk}W_{kl,z}V_l & z_{lk}W_{kl,z}V_l \end{bmatrix} \begin{bmatrix} f_k \\ f_{k,x} \\ f_{k,y} \\ f_{k,z} \end{bmatrix} = \begin{bmatrix} f_l W_{kl}V_l \\ f_l W_{kl,x}V_l \\ f_l W_{kl,y}V_l \\ f_l W_{kl,z}V_l \end{bmatrix}, \quad (\text{A.5})$$

where,  $k$  is the destination particle index,  $l$  is the neighbor particle index,  $W_{kl,\beta}$  for  $\beta \in x, y, z$  is the kernel gradient component in the  $\beta$  direction. All the terms containing  $l$  are summed over all the neighbor particles. On solving the eq. (A.5), we obtain a first order consistent gradient [10]. For a constant field, this method ensures that we satisfy  $\sum W_{ij}\omega_j = 1$  and  $\sum \nabla W_{ij}\omega_j = 0$ . Therefore, with this correction in both the **sym1** and **asym** forms the second term becomes zero, and we get the SOC approximation. Whereas, in **sym2** the term  $p_i/\rho_i^2$  does not become zero, thus even this correction fails to correct the approximation.

## Appendix B. The divergence-free velocity field

In this section, we explain the reason behind the astonishing accuracy obtained when evaluating the divergence of a divergence-free field using a fixed Cartesian mesh of particles as discussed in section 4.2. We consider a 2-dimensional velocity field. We write the error  $Er$ , in the divergence evaluation as

$$Er_i = \nabla \cdot \mathbf{u} - \sum_j (\mathbf{u}_j - \mathbf{u}_i) \cdot \nabla W_{ij}\omega_j, \quad (\text{B.1})$$

Using first order Taylor-series expansion of  $\mathbf{u}_j$  about the point  $\mathbf{x}_i$ ,

$$\mathbf{u}_j = \mathbf{u}_i - (\mathbf{x}_{ij} \cdot \nabla) \mathbf{u}_i. \quad (\text{B.2})$$

We write,

$$\begin{aligned} Er_i = & \left(1 - \sum_j x_{ij} \frac{\partial W_{ij}}{\partial x} \omega_j\right) \frac{\partial u_i}{\partial x} + \left(1 - \sum_j y_{ij} \frac{\partial W_{ij}}{\partial y} \omega_j\right) \frac{\partial v_i}{\partial y} \\ & - \sum_j y_{ij} \frac{\partial u_i}{\partial y} \frac{\partial W_{ij}}{\partial x} \omega_j - \sum_j x_{ij} \frac{\partial v_i}{\partial x} \frac{\partial W_{ij}}{\partial y} \omega_j. \end{aligned} \quad (\text{B.3})$$

In the case of a UP domain, in eq. (B.3), the last two terms are exactly zero and the coefficient of the first two terms are of equal magnitude. Furthermore, since for the divergence-free velocity field,  $\frac{\partial u_i}{\partial x} = -\frac{\partial v_i}{\partial y}$ , the overall error becomes zero. On the other hand, in a PP domain, the last two terms are of equal magnitude thus cancel, and the first two terms are different to the order  $10^{-4}$  which becomes the leading error term. Thus, we always get the error of the order  $10^{-4}$  even after applying the Bonet correction. As far as we are aware there are no known SPH discretizations which can resolve this issue using a simple correction as done in case of gradients. This is a possible avenue for future research.

### Appendix C. The Cleary and Fatehi corrections

In this section, we introduce the tensor notations for SPH that makes the comprehension better. We use derivation for the error estimation from Fatehi and Manzari [27]. We write the Taylor series expansion of the velocity component,  $u_j$  defined at a point,  $\mathbf{x}_j$  about a point  $x_i$  as, expansion given by

$$u_j = u_i - (\mathbf{x}_{ij} \cdot \nabla)u_i + \frac{1}{2}(\mathbf{x}_{ij} \cdot \nabla)^2 u_i - \frac{1}{6}(\mathbf{x}_{ij} \cdot \nabla)^3 u_i + \text{H.O.T} \quad (\text{C.1})$$

where,  $\mathbf{x}_{ij} = \mathbf{x}_i - \mathbf{x}_j$ . Without loss of generality, we consider only one component of velocity. We use tensor notation to represent vector  $\mathbf{x}_{ij}$  as  $x_{ij}^\alpha$ , where  $i$  and  $j$  are the particle indices. We follow this notation since SPH approximation is performed using sum over all its neighbors  $j$ . Thus, we write the eq. (C.1) in this tensor notation as

$$u_j = u_i - x_{ij}^\alpha \partial^\alpha u_i + \frac{1}{2} x_{ij}^\beta x_{ij}^\gamma \partial^\beta \partial^\gamma u_i - \frac{1}{6} x_{ij}^\alpha x_{ij}^\beta x_{ij}^\gamma \partial^\alpha \partial^\beta \partial^\gamma u_i + \text{H.O.T.} \quad (\text{C.2})$$

We note that the subscripts are SPH notations and the superscripts are tensor notation indices.

We write the Laplacian of velocity,  $\mathbf{u}$  using proposed by [26] as

$$\langle \partial^\eta \partial^\eta u \rangle_i = \sum_j 2\omega_j (u_i - u_j) \frac{\partial^\eta W_{ij} x_{ij}^\eta}{r_{ij}^2} \quad (\text{C.3})$$

where  $\langle * \rangle$  is used to denote the approximation. We write the error,  $E_i$  in the approximation as

$$E_i = \partial^\eta \partial^\eta u_i - \langle \partial^\eta \partial^\eta u \rangle_i \quad (\text{C.4})$$

Using eq. (C.2) and eq. (C.3), we obtain the error,

$$E_i = \partial^\theta \partial^\theta u_i - \sum_j 2\omega_j [x_{ij}^\alpha \partial^\alpha u_i - \frac{1}{2} x_{ij}^\beta x_{ij}^\gamma \partial^\beta \partial^\gamma u_i + \frac{1}{6} x_{ij}^\delta x_{ij}^\epsilon x_{ij}^\zeta \partial^\delta \partial^\epsilon \partial^\zeta u_i + \text{H.O.T}] \frac{\partial^\eta W_{ij} x_{ij}^\eta}{r_{ij}^2}. \quad (\text{C.5})$$

In the above equation, we can write  $\partial^\theta \partial^\theta u_i = \delta^{\theta\iota} \partial^\theta \partial^\iota u_i$  and multiplying each term inside, we get,

$$E_i = -\partial^\alpha u_i \sum_j 2\omega_j e_{ij}^\alpha e_{ij}^\eta \partial^\eta W_{ij} + \left( \delta^{\beta\gamma} + \sum_j \omega_j x_{ij}^\beta x_{ij}^\gamma \frac{\partial^\eta W_{ij} x_{ij}^\eta}{r_{ij}^2} \right) \partial^\beta \partial^\gamma u_i + \text{H.O.T} \quad (\text{C.6})$$

We can see that the first term is leading error term in the above equation. For a smoothing kernel,  $W$  the term,

$$\sum_j \omega_j (\mathbf{x}_{ij} \otimes \mathbf{x}_{ij}) \nabla W_{ij} \quad (\text{C.7})$$

is the second moment of the kernel gradient. In a UP domain, the second moment is zero. However, the leading term of the error is second moment scaled by  $\frac{1}{|x_{ij}|^2}$  which is still zero since it is a constant in a UP domain. Whereas, the leading term is non-zero and causes the approximation to deviate.

In the modified formulation proposed by Fatehi and Manzari [27], the leading term is included in the approximation. We write the modified form as

$$\langle \partial^\theta \partial^\theta u_i \rangle_i = \sum_j 2\omega_j ((u_i - u_j) - x_{ij}^\alpha \langle \partial^\alpha u \rangle_i) \frac{\partial^\eta W_{ij} x_{ij}^\eta}{r_{ij}^2} \quad (\text{C.8})$$

Using the similar algebraic manipulation, we write the error term as

$$E_i = \left( \sum_j \omega_j x_{ij}^\beta x_{ij}^\gamma \partial^\theta W_{ij} B_i^{T, \theta\alpha} \sum_j \omega_j e_{ij}^\alpha e_{ij}^\eta \partial^\eta W_{ij} + \delta^{\beta\gamma} + \sum_j \omega_j x_{ij}^\beta x_{ij}^\gamma \frac{\partial^\eta W_{ij} x_{ij}^\eta}{r_{ij}^2} \right) \partial^\beta \partial^\gamma u_i + \text{H.O.T} \quad (\text{C.9})$$

where  $B^T$  is the correction matrix in eq. (A.1). Fatehi and Manzari [27] also proposed a correction for the kernel gradient. Let us assume the correction  $\hat{B}_i^{\eta\mu}$  is applied to the kernel gradient. We write the modified equation as

$$\langle \partial^\theta \partial^\theta u_i \rangle_i = \sum_j 2\omega_j ((u_i - u_j) - x_{ij}^\alpha \langle \partial^\alpha u \rangle_i) \frac{\hat{B}_i^{\eta\mu} \partial^\mu W_{ij} x_{ij}^\eta}{r_{ij}^2} \quad (\text{C.10})$$

The Error in the above equation is given by

$$E_i = \left( \sum_j \omega_j x_{ij}^\beta x_{ij}^\gamma \partial^\theta W_{ij} B_i^{T,\theta\alpha} \sum_j \omega_j e_{ij}^\alpha e_{ij}^\eta \hat{B}_i^{\eta\mu} \partial^\mu W_{ij} + \delta^{\beta\gamma} + \sum_j \omega_j x_{ij}^\beta x_{ij}^\gamma \frac{\hat{B}_i^{\eta\mu} \partial^\mu W_{ij} x_{ij}^\eta}{r_{ij}^2} \right) \partial^\beta \partial^\gamma u_i + \text{H.O.T} \quad (\text{C.11})$$

In order to make the approximation second order accurate, we must have the coefficient of  $\partial^\beta \partial^\gamma u_i$  equal to zero. Thus we get,

$$\sum_j \omega_j x_{ij}^\beta x_{ij}^\gamma \partial^\theta W_{ij} B_i^{T,\theta\alpha} \sum_j \omega_j e_{ij}^\alpha e_{ij}^\eta \hat{B}_i^{\eta\mu} \partial^\mu W_{ij} + \sum_j \omega_j e_{ij}^\beta e_{ij}^\gamma \hat{B}_i^{\eta\mu} \partial^\mu W_{ij} x_{ij}^\eta = -\delta^{\beta\gamma} \quad (\text{C.12})$$

On inverting the system, we obtain,

$$\hat{B}_i^{\eta\mu} = - \left( \sum_j \omega_j \partial^\mu W_{ij} x_{ij}^\eta + \sum_j \omega_j r_{ij}^2 \partial^\theta W_{ij} B_i^{T,\theta\alpha} \sum_j \omega_j e_{ij}^\alpha e_{ij}^\eta \partial^\mu W_{ij} \right)^{-1} \quad (\text{C.13})$$

The above equation is the correction matrix proposed by [27] in a simple tensorial notation.

#### Appendix D. $\delta^+$ -SPH formulation correction

The the evolution equation of the  $\delta^+$ -SPH equation has the form

$$\frac{Df}{Dt} = \frac{df}{dt} + \nabla f \cdot \delta \mathbf{u}, \quad (\text{D.1})$$

where  $\frac{Df}{Dt} = \frac{\partial f}{\partial t} + (\mathbf{u} + \delta \mathbf{u}) \cdot \nabla f$ . The above equation can be written in terms of a particle  $i$  as,

$$\frac{Df_i}{Dt} = \frac{df_i}{dt} + \nabla f_i \cdot \delta \mathbf{u}_i. \quad (\text{D.2})$$

We can use the vector identity for the last term,

$$\nabla f \cdot \delta \mathbf{u} = \nabla \cdot (f \delta \mathbf{u}) - f \nabla \cdot (\delta \mathbf{u}). \quad (\text{D.3})$$

On performing SPH approximation, we obtain

$$\begin{aligned} \nabla f_i \cdot \delta \mathbf{u}_i &= \sum_j (f_j \delta \mathbf{u}_j - f_i \delta \mathbf{u}_i) \cdot \nabla W_{ij} \omega_j - \sum_j f_i (\delta \mathbf{u}_j - \delta \mathbf{u}_i) \cdot \nabla W_{ij} \omega_j \\ &= \sum_j (f_j - f_i) \delta \mathbf{u}_j \cdot \nabla W_{ij} \omega_j. \end{aligned} \quad (\text{D.4})$$

Clearly, we cannot recover the LHS should we use the above discretization. However, on using  $f_j$  in place of  $f_i$  in the second term, we get

$$\begin{aligned} \nabla f_i \cdot \delta \mathbf{u}_i &= \sum_j (f_j \delta \mathbf{u}_j - f_i \delta \mathbf{u}_i) \cdot \nabla W_{ij} \omega_j - \sum_j f_j (\delta \mathbf{u}_j - \delta \mathbf{u}_i) \cdot \nabla W_{ij} \omega_j \\ &= \sum_j (f_j - f_i) \delta \mathbf{u}_i \cdot \nabla W_{ij} \omega_j. \end{aligned} \quad (\text{D.5})$$

Thus, in the  $\delta^+$ -SPH we should use the above discretization.

## Appendix E. Schemes with issues solving the Gresho-Chan vortex

In this section, we show the results for the scheme for which the Gresho-Chan vortex problem failed to complete. In fig. E.21, we plot the velocity of the particles with the distance,  $r$  from the center at  $t = 1.5s$ , and the linear momentum in the x-direction with time for a  $100 \times 100$  simulation. Clearly, all the schemes considered show better approximate conservation of linear momentum compared to other scheme; however, they fail to complete.

In case of L-RR-C, due to the present of sharp change in the velocity field, the remeshing procedure diverges [39]. In case of E-C, TV-C and EWCSPH, we suspect that the advection term  $\mathbf{u} \cdot \nabla \mathbf{u}$  (or  $\delta \mathbf{u} \cdot \nabla \mathbf{u}$  in case of TV-C) diverge in the absence of viscosity. This opens possible avenues of research to obtain a better discretization of the advection term.

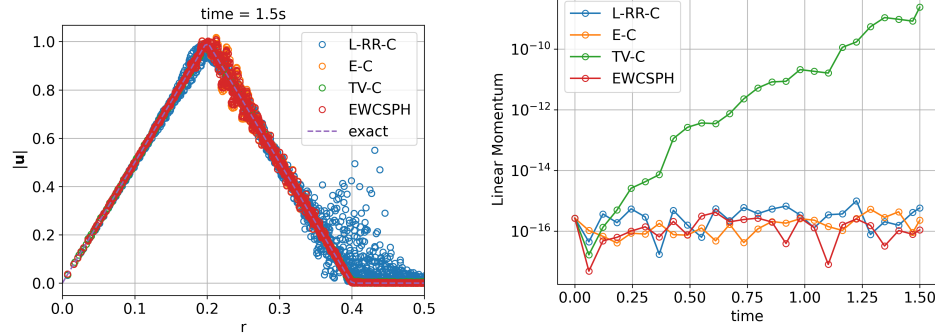


Figure E.21: The velocity of particles with the distance from the center of the vortex (left) and the  $x$ -component of the total linear momentum (right) for the Gresho-Chan vortex problem.

## References

## References

1. Monaghan, J.J.. Simulating free surface flows with SPH. *Journal of Computational Physics* 1994;110:399–406. doi:10.1006/jcph.1994.1034.
2. Vacondio, R., Altomare, C., De Lefte, M., Hu, X., Le Touzé, D., Lind, S., Marongiu, J.C., Marrone, S., Rogers, B.D., Souto-Iglesias, A.. Grand challenges for Smoothed Particle Hydrodynamics numerical schemes. *Computational Particle Mechanics* 2020;doi:10.1007/s40571-020-00354-1.
3. Hernquist, L., Katz, N.. TREESPH-A unification of SPH with the hierarchical tree method. *The Astrophysical Journal Supplement Series* 1989;70:419–446. doi:10.1086/191344.
4. Quinlan, N.J., Basa, M., Lastiwka, M.. Truncation error in mesh-free particle methods. *International Journal for Numerical Methods in Engineering* 2006;66(13):2064–2085. doi:10.1002/nme.1617.
5. Zhu, Q., Hernquist, L., Li, Y.. Numerical convergence in smoothed particle hydrodynamics. *The Astrophysical Journal* 2015;800(1):6. doi:10.1088/0004-637X/800/1/6.

6. Kiara, A., Hendrickson, K., Yue, D.K.. SPH for incompressible free-surface flows. Part I: Error analysis of the basic assumptions. *Computers & Fluids* 2013;86:611–624. doi:10.1016/j.compfluid.2013.05.023.
7. Kiara, A., Hendrickson, K., Yue, D.K.P.. SPH for incompressible free-surface flows. Part II: Performance of a modified SPH method. *Computers & Fluids* 2013;86:510–536. doi:10.1016/j.compfluid.2013.07.016.
8. Lind, S.J., Stansby, P.K.. High-order Eulerian incompressible smoothed particle hydrodynamics with transition to Lagrangian free-surface motion. *Journal of Computational Physics* 2016;326:290–311. doi:10.1016/j.jcp.2016.08.047.
9. Bonet, J., Lok, T.S.. Variational and momentum preservation aspects of smooth particle hydrodynamic formulations. *Computer Methods in Applied Mechanics and Engineering* 1999;180(1):97 – 115. doi:10.1016/S0045-7825(99)00051-1.
10. Liu, M., Liu, G.. Restoring particle consistency in smoothed particle hydrodynamics. *Applied Numerical Mathematics* 2006;56(1):19–36. doi:10.1016/j.apnum.2005.02.012.
11. Rosswog, S.. Boosting the accuracy of SPH techniques: Newtonian and special-relativistic tests. *Monthly Notices of the Royal Astronomical Society* 2015;448(4):3628–3664. doi:10.1093/mnras/stv225.
12. Huang, C., Long, T., Li, S., Liu, M.. A kernel gradient-free sph method with iterative particle shifting technology for modeling low-reynolds flows around airfoils. *Engineering Analysis with Boundary Elements* 2019;106:571–587. doi:10.1016/j.enganabound.2019.06.010.
13. Adami, S., Hu, X., Adams, N.. A transport-velocity formulation for smoothed particle hydrodynamics. *Journal of Computational Physics* 2013;241:292–307. doi:10.1016/j.jcp.2013.01.043.
14. Monaghan, J.J., Gingold, R.A.. Shock simulation by the particle method SPH. *Journal of computational physics* 1983;52(2):374–389. doi:10.1016/0021-9991(83)90036-0.



15. Violeau, D.. Fluid mechanics and the SPH method: theory and applications. Oxford University Press; 2012. doi:10.1093/acprof:oso/9780199655526.001.0001.
16. Frontiere, N., Raskin, C.D., Owen, J.M.. CRKSPH - a conservative reproducing kernel smoothed particle hydrodynamics scheme. *Journal of Computational Physics* 2017;332(1):160–209. doi:10.1016/j.jcp.2016.12.004.
17. Dilts, G.A.. Moving-least-squares-particle hydrodynamics—I. consistency and stability. *International Journal for Numerical Methods in Engineering* 1999;44(8):1115–1155. doi:10.1002/(SICI)1097-0207(19990320)44:8<1115::AID-NME547>3.0.CO;2-L.
18. Dilts, G.A.. Moving least-squares particle hydrodynamics II: conservation and boundaries. *International Journal for numerical methods in engineering* 2000;48(10):1503–1524. doi:10.1002/1097-0207(20000810)48:10<1503::AID-NME832>3.0.CO;2-D.
19. Chen, J.K., Beraun, J.E.. A generalized smoothed particle hydrodynamics method for nonlinear dynamic problems. *Computer Methods in Applied Mechanics and Engineering* 2000;190(1):225–239. doi:10.1016/S0045-7825(99)00422-3.
20. Zhang, G.M., Batra, R.C.. Modified smoothed particle hydrodynamics method and its application to transient problems. *Computational Mechanics* 2004;34(2):137–146. doi:10.1007/s00466-004-0561-5.
21. Korzilius, S.P., Schilders, W.H.A., Anthonissen, M.J.H.. An Improved CSPM Approach for Accurate Second-Derivative Approximations with SPH. *Journal of Applied Mathematics and Physics* 2017;05(01):168–184. doi:10.4236/jamp.2017.51017.
22. Schwaiger, H.F.. An implicit corrected SPH formulation for thermal diffusion with linear free surface boundary conditions. *International Journal for Numerical Methods in Engineering* 2008;75(6):647–671. doi:10.1002/nme.2266.
23. Macià, F., González, L.M., Cercos-Pita, J.L., Souto-Iglesias, A.. A Boundary Integral SPH Formulation: Consistency and Applications to

- ISPH and WCSPH. *Progress of Theoretical Physics* 2012;128(3):439–462. doi:10.1143/PTP.128.439.
24. Brookshaw, L.. A Method of Calculating Radiative Heat Diffusion in Particle Simulations. *Publications of the Astronomical Society of Australia* 1985;6(2):207–210. doi:10.1017/S1323358000018117.
  25. Morris, J.P., Fox, P.J., Zhu, Y.. Modeling low reynolds number incompressible flows using SPH. *Journal of Computational Physics* 1997;136(1):214–226. doi:10.1006/jcph.1997.5776.
  26. Cleary, P.W., Monaghan, J.J.. Conduction modelling using smoothed particle hydrodynamics. *Journal of Computational Physics* 1999;148(1):227–264. doi:10.1006/jcph.1998.6118.
  27. Fatehi, R., Manzari, M.. Error estimation in smoothed particle hydrodynamics and a new scheme for second derivatives. *Computers & Mathematics with Applications* 2011;61(2):482–498. doi:10.1016/j.camwa.2010.11.028.
  28. Nugent, S., Posch, H.A.. Liquid drops and surface tension with smoothed particle applied mechanics. *Physical Review E* 2000;62(4):4968–4975. doi:10.1103/PhysRevE.62.4968; publisher: American Physical Society.
  29. Biriukov, S., Price, D.J.. Stable anisotropic heat conduction in smoothed particle hydrodynamics. *Monthly Notices of the Royal Astronomical Society* 2019;483(4):4901–4909. doi:10.1093/mnras/sty3413.
  30. Gomez-Gesteria, M., Rogers, B.D., Dalrymple, R.A., Crespo, A.J.. State-of-the-art classical SPH for free-surface flows. *Journal of Hydraulic Research* 2010;84:6–27. doi:10.1080/00221686.2010.9641242.
  31. Xu, R., Stansby, P., Laurence, D.. Accuracy and stability in incompressible sph (ISPH) based on the projection method and a new approach. *Journal of Computational Physics* 2009;228(18):6703–6725. doi:10.1016/j.jcp.2009.05.032.
  32. Lind, S.J., Xu, R., Stansby, P.K., Rogers, B.D.. Incompressible smoothed particle hydrodynamics for free-surface flows: A generalised diffusion-based algorithm for stability and validations for impul-

- sive flows and propagating waves. *Journal of Computational Physics* 2012;231(4):1499–1523. doi:10.1016/j.jcp.2011.10.027.
33. Sun, P., Colagrossi, A., Marrone, S., Antuono, M., Zhang, A.M.. A consistent approach to particle shifting in the  $\delta$  - Plus -SPH model. *Computer Methods in Applied Mechanics and Engineering* 2019;348:912–934. doi:10.1016/j.cma.2019.01.045.
  34. Oger, G., Marrone, S., Le Touzé, D., de Lefte, M.. SPH accuracy improvement through the combination of a quasi-Lagrangian shifting transport velocity and consistent ALE formalisms. *Journal of Computational Physics* 2016;313:76–98. doi:10.1016/j.jcp.2016.02.039.
  35. Marrone, S., Antuono, M., Colagrossi, A., Colicchio, G., Le Touzé, D., Graziani, G..  $\delta$ -SPH model for simulating violent impact flows. *Computer Methods in Applied Mechanics and Engineering* 2011;200:1526–1542. doi:10.1016/j.cma.2010.12.016.
  36. Antuono, M., Colagrossi, A., Marrone, S., Molteni, D.. Free-surface flows solved by means of SPH schemes with numerical diffusive terms. *Computer Physics Communications* 2010;181(3):532 – 549. doi:10.1016/j.cpc.2009.11.002.
  37. Ramachandran, P., Puri, K.. Entropically damped artificial compressibility for SPH. *Computers and Fluids* 2019;179(30):579–594. doi:10.1016/j.compfluid.2018.11.023.
  38. Clausen, J.R.. Entropically damped form of artificial compressibility for explicit simulation of incompressible flow. *Physical Review E* 2013;87(1):013309–1–013309–12. doi:10.1103/PhysRevE.87.013309.
  39. Chaniotis, A., Poulikakos, D., Koumoutsakos, P.. Remeshed smoothed particle hydrodynamics for the simulation of viscous and heat conducting flows. *Journal of Computational Physics* 2002;182(1):67 – 90. doi:10.1006/jcph.2002.7152.
  40. Hieber, S.E., Koumoutsakos, P.. An immersed boundary method for smoothed particle hydrodynamics of self-propelled swimmers. *Journal of Computational Physics* 2008;227(19):8636–8654. doi:10.1016/j.jcp.2008.06.017.

41. Nasar, A., Rogers, B., Revell, A., Stansby, P., Lind, S.. Eulerian weakly compressible smoothed particle hydrodynamics (SPH) with the immersed boundary method for thin slender bodies. *Journal of Fluids and Structures* 2019;84:263–282. doi:10.1016/j.jfluidstructs.2018.11.005.
42. Sun, P., Colagrossi, A., Marrone, S., Antuono, M., Zhang, A.M.. A consistent approach to particle shifting in the  $\delta$ -plus-sph model. *Computer Methods in Applied Mechanics and Engineering* 2019;348:912–934. doi:10.1016/j.cma.2019.01.045.
43. Lind, S., Xu, R., Stansby, P., Rogers, B.. Incompressible smoothed particle hydrodynamics for free-surface flows: A generalised diffusion-based algorithm for stability and validations for impulsive flows and propagating waves. *Journal of Computational Physics* 2012;231(4):1499 – 1523. doi:10.1016/j.jcp.2011.10.027.
44. Dehnen, W., Aly, H.. Improving convergence in smoothed particle hydrodynamics simulations without pairing instability. *Monthly Notices of the Royal Astronomical Society* 2012;425(2):1068–1082. doi:10.1111/j.1365-2966.2012.21439.x.
45. Gresho, P.M., Chan, S.T.. On the theory of semi-implicit projection methods for viscous incompressible flow and its implementation via a finite element method that also introduces a nearly consistent mass matrix. part 2: Implementation. *International journal for numerical methods in fluids* 1990;11(5):621–659. doi:10.1002/flid.1650110510.
46. Di, Y., Li, R., Tang, T., Zhang, P.. Moving Mesh Finite Element Methods for the Incompressible Navier–Stokes Equations. *SIAM Journal on Scientific Computing* 2005;26(3):1036–1056. doi:10.1137/030600643.
47. Ramachandran, P.. automan: A python-based automation framework for numerical computing. *Computing in Science & Engineering* 2018;20(5):81–97. doi:10.1109/MCSE.2018.05329818.
48. Monaghan, J.J.. Smoothed Particle Hydrodynamics. *Reports on Progress in Physics* 2005;68:1703–1759. doi:10.1088/0034-4885/68/8/R01.

49. Wendland, H.. Piecewise polynomial, positive definite and compactly supported radial functions of minimal degree. *Advances in Computational Mathematics* 1995;4(1):389–396. doi:10.1007/BF02123482.
50. Randles, P., Libersky, L.D.. Smoothed particle hydrodynamics: some recent improvements and applications. *Computer methods in applied mechanics and engineering* 1996;139(1-4):375–408. doi:10.1016/S0045-7825(96)01090-0.
51. Negi, P., Ramachandran, P.. Algorithms for uniform particle initialization in domains with complex boundaries. *Computer Physics Communications* 2021;265:108008. doi:10.1016/j.cpc.2021.108008.
52. Colagrossi, A., Bouscasse, B., Antuono, M., Marrone, S.. Particle packing algorithm for SPH schemes. *Computer Physics Communications* 2012;183(8):1641–1653. doi:10.1016/j.cpc.2012.02.032.
53. Monaghan, J.J.. SPH without a tensile instability. *Journal of Computational Physics* 2000;159:290–311. doi:10.1006/jcph.2000.6439.
54. Nguyen, V.P., Rabczuk, T., Bordas, S., Dufloy, M.. Meshless methods: A review and computer implementation aspects. *Mathematics and Computers in Simulation* 2008;79(3):763–813. doi:10.1016/j.matcom.2008.01.003.
55. Sun, P.N., Colagrossi, A., Zhang, A.M.. Numerical simulation of the self-propulsive motion of a fishlike swimming foil using the  $\delta$ -sph model. *Theoretical and Applied Mechanics Letters* 2018;8(2):115–125. doi:10.1016/j.taml.2018.02.007.
56. Sun, P., Colagrossi, A., Marrone, S., Zhang, A.. The  $\delta$ plus-sph model: Simple procedures for a further improvement of the sph scheme. *Computer Methods in Applied Mechanics and Engineering* 2017;315:25–49. doi:10.1016/j.cma.2016.10.028.
57. Zhang, C., Hu, X.Y.T., Adams, N.A.. A generalized transport-velocity formulation for smoothed particle hydrodynamics. *Journal of Computational Physics* 2017;337:216–232. doi:10.1016/j.jcp.2017.02.016.

58. Shao, S., Lo, E.Y.. Incompressible SPH method for simulating newtonian and non-newtonian flows with a free surface. *Advances in Water Resources* 2003;26(7):787 – 800. doi:10.1016/S0309-1708(03)00030-7.
59. Oger, G., Doring, M., Alessandrini, B., Ferrant, P.. An improved SPH method: Towards higher order convergence. *Journal of Computational Physics* 2007;225(2):1472–1492. doi:10.1016/j.jcp.2007.01.039.
60. Chorin, A.J.. A numerical method for solving incompressible viscous flow problems. *Journal of Computational Physics* 1967;2(1):12–26. doi:10.1016/0021-9991(67)90037-X.
61. Fatehi, R., Rahmat, A., Tofighi, N., Yildiz, M., Shadloo, M.S.. Density-based smoothed particle hydrodynamics methods for incompressible flows. *Computers & Fluids* 2019;185:22–33. doi:10.1016/j.compfluid.2019.02.018.
62. Ramachandran, P., Muta, A., Ramakrishna, M.. Dual-time smoothed particle hydrodynamics for incompressible fluid simulation. *Computers & Fluids* 2021;227:105031. doi:10.1016/j.compfluid.2021.105031.
63. Ramachandran, P., Bhosale, A., Puri, K., Negi, P., Muta, A., Adepu, D., Menon, D., Govind, R., Sanka, S., Sebastian, A.S., Sen, A., Kaushik, R., Kumar, A., Kurapati, V., Patil, M., Tavker, D., Pandey, P., Kaushik, C., Dutt, A., Agarwal, A.. PySPH: a Python-based framework for smoothed particle hydrodynamics. *arXiv preprint arXiv:190904504* 2020;URL: <https://arxiv.org/abs/1909.04504>.